JOURNAL OF MATERIALS SCIENCE 21 (1986) 1377–1397

Microstructural evolution in reaction-bonded silicon carbide

J. N. NESS, T. F. PAGE
Department of Metallurgy and Materials Science, University of Cambridge, Pembroke Street, Cambridge CB2 3QZ, UK

A detailed microstructural investigation of reaction-bonded silicon carbide has been performed using both fully-bonded and quenched samples and other specially prepared specimens containing large original single crystals of known crystallographic habit. The development of the epitaxial SiC overgrowth on the original SiC particles has been followed and found to proceed by the progressive growth and coalescence of identically-oriented nuclei. This epitaxial layer grows with a habit characteristic of β (cubic) SiC and then transforms to α-SiC in the high temperature region behind the reaction front. The formation of faceted grain boundaries is explained by this growth morphology. Furthermore, SiC:SiC grain boundaries, SiC:SiC epitaxial boundaries and SiC:Si interfaces have all been characterized by TEM techniques. The grain boundaries are of particular interest since they usually comprise a thin ($\sim$1 nm) layer of amorphous SiC with occasional silicide and graphite inclusions. The general cleanliness of the vast majority of interfacial area is a result of the removal of the impurities insoluble in SiC by liquid silicon moving through the sample. The overall distribution of impurities is discussed. Other microstructural features have been characterized and texturing due to original particle alignment during fabrication of the green compact investigated. The control of the mechanical properties of reaction-bonded silicon carbide by these various microstructural features is discussed. A basis for an explanation of the interesting trace-impurity-controlled contrast seen in secondary electron images of these materials is also established.

1. Introduction

Reaction-bonded silicon carbides are fully dense engineering ceramics formed by the bonding together of silicon carbide powders with further silicon carbide produced *in situ* by a chemical reaction between silicon and carbon. They are used extensively in applications where wear-resistance is required, often at high temperatures and in hostile environments (e.g. [1]). The mechanical properties of such materials (e.g. strength, hardness, fracture paths), at both ambient and elevated temperatures, are known to be sensitive to a range of microstructural features (e.g. [2]). This paper presents the results of a detailed examination of the microstructural genesis and final microstructural features in one such material, REFEL* silicon carbide. This particular material was initially developed by Popper [3] at the British Ceramic Research Association, and was subsequently developed at UKAEA Springfields as a high-temperature nuclear fuel cladding material [4], whence it has found various other uses as bearing, dies and seals, etc. (e.g. [1]).

Fabrication of REFEL silicon carbide involves the forming of a compact of silicon carbide, graphite and a polymeric binder by various standard polymer forming routes such as extrusion and pressing. The compact is then heated in air to remove the binder and the resulting porous compact infiltrated with liquid silicon in a radio-frequency heated (RF) furnace. The liquid silicon rises through the porous material by capillary action, reacting with the graphite to form "new" silicon carbide which "bonds" the material together. The final material consists of a matrix of silicon carbide, with 10 to 15% silicon occupying the residual pore space necessary for full penetration of the silicon into the compact. This process has been fully described elsewhere (e.g. [4]).

The final microstructure was originally described by both Popper [3] and Forrest *et al.* [4] as consisting of large (10 to 20 μm) grains of α-SiC† (the original silicon carbide) bonded together by fine β-SiC, which was produced from the reaction of carbon with liquid silicon. Later, Sato *et al.* [6] working on similar material, reported that the silicon carbide produced in the process deposited epitaxially as β-SiC on the original material with a certain amount of fine β-SiC also being independently nucleated. Other workers [7, 8] confirmed this basic distribution of new silicon carbide, but found that the epitaxial material was almost

---

*REFEL silicon carbide is a registered trademark of UKAEA Springfields.

†α-SiC refers collectively to all the hexagonal and rhombohedral polytypes of silicon carbide, β-SiC being reserved for the cubic polytype. This notation will be used throughout the rest of this paper, as will the Ramsdell notation [5] which describes the polytype by a number representing the c-axis layer repeat and a letter representing the lattice type (e.g. 6H, 15R, 3C).

0022–2461/86 $03.00 + .12

exclusively α-SiC, suggesting that the $\beta \rightarrow \alpha$ transformation had occurred to produce grains with a uniform crystal structure over most of their bulk [9, 10]. This behaviour was confirmed by Ness and Page [11], who found that the $\beta \rightarrow \alpha$ transformation occurred largely due to the localized heating in the reaction zone, caused by the exothermic nature of the reaction-bonding process.

The reaction mechanism proposed by Sawyer and Page [7] was the precipitation of silicon carbide from a supersaturated solution of graphite in liquid silicon on to local nucleation sites (such as the original silicon carbide grits and/or the graphite). The heat evolved in the reaction accelerated the rate of carbon dissolution and allowed the reaction to go to rapid local completion. The reaction was assumed to be confined to a narrow band just behind the rising silicon front where the temperature rises by several hundred degrees Kelvin, but the effects of local temperature gradients within this region were not clear. The bulk strength of the material was thought to derive from the SiC:SiC grain boundaries formed between epitaxial material, with the independently nucleated fine β-SiC (when present) contributing little or nothing to the strength, due to its small grain boundary area.

This paper expands on these initial findings and, in the light of further experimental results, is now able to describe both the microstructural evolution and final microstructural features in much greater detail. Particular emphasis is placed on the nucleation and growth of the new material, the various types of interface produced – especially grain boundaries – and the distribution of impurities.

2. Experimental details

All the materials used in this study were produced at UKAEA Springfields. In addition to standard production material, several special samples were produced by interrupting the reaction-bonding process, by quenching in argon and in water. Furthermore, some samples had large (100 μm to 5 mm) Acheson-type silicon carbide crystals incorporated into the initial compact. These crystals provided reference substrates of known crystallographic orientation, morphology and purity, and also enabled the effects of extreme grit size to be studied.

Sections were cut using a Capco Q35, Mark II diamond saw and polished on various diamond laps and cloths (e.g. [2]). Some specimens were broken along "silicon cracks" (cracks in the initial compact now filled with silicon) and the silicon network removed using an $HF{:}6HNO_3$ etchant [6]. All specimens were examined (uncoated) by light microscopy and by both secondary electron and backscattered electron imaging in a Stereoscan SII and a Camscan S4 scanning electron microscopes (SEMs). X-ray diffractometry was performed on a standard Philips vertical diffractometer, with Cu$K\alpha$ radiation, another copper source being used for Laue photography. Energy dispersive X-ray spectroscopy (EDS) analyses were undertaken using a Link Systems 860 Mark III analyser on an ISI 100A SEM, which was also used for selected-area channelling.

Transmission electron microscopy (TEM) foils were polished to $\leq 100\,\mu m$ thickness, 3 and 2.3 mm discs cut with a Kerry Sonorode 150 Ultrasonic drill, and then ion-beam thinned to perforation on an Edwards IBMA2 ion-beam thinner. The specimens were observed in a variety of instruments (e.g. Philips 400T, 400ST; JEOL 120CX; Cambridge HREM), some of which had facilities for chemical microanalysis by electron energy loss spectroscopy (EELS) and EDS. Auger analyses were performed at UKAEA Springfields. Linear grain intercept measurements were performed using a Quantimet 720B on carefully prepared tracings from scanning electron micrographs.

3. Nucleation and growth of new material

In order to facilitate the description and later discussion of the microstructure, Fig. 1 shows SEM backscattered electron (BEI) and secondary electron (SEI) images of a polished uncoated sample of REFEL silicon carbide, in which the new silicon carbide is almost exclusively epitaxial on the original silicon carbide grits. Also shown is a schematic diagram (Fig. 1c) of four grains, with various microstructural features labelled, including the different types of interface present and epitaxial coatings in various stages of transformation. The BEI (Fig. 1a) differentiates the silicon and silicon carbide by atomic number contrast, the silicon appearing lighter. Some electron channelling contrast is also present, which helps to distinguish the individual silicon carbide crystals. The SEI image of Fig. 1b reveals the internal structure of the silicon carbide grains, each grain typically comprising a darker-imaging angular core (the original grit particle), with a lighter-imaging coating which may also contain other shades of grey (the epitaxial coating). Sawyer and Page [7] used this trace-impurity-controlled secondary electron contrast to differentiate between "old" and "new" silicon carbide and suggested that the lighter-imaging areas consisted of purer material.

Fig. 2 is an SEI of a fractured, unsilicided compact and shows a uniform distribution of initial ($\sim 10\,\mu m$) silicon carbide grits and fine ($\leq 1\,\mu m$) graphite flakes. During reaction-bonding, liquid silicon rises through such compacts, the infiltration rate often being enhanced by the presence of a highly porous carbon-free surface layer (the "burn-out" layer [4]).

3.1. The reaction mechanism

The reaction commences as soon as the molten silicon (melting point ~ 1410° C) is sufficiently fluid to allow it to rise through the compact, its viscosity being quite high initially but falling with increasing temperature [12]. The bulk specimen temperature is allowed to rise to a steady-state value of 1600 to 1650° C and therefore, the first-formed material will have reacted at a lower overall temperature than this. The silicon rises quite rapidly through the compact, the rate of rise depending on the size of the pores, the height of the silicon in the specimen, the viscosity of the silicon and the extent to which it wets the silicon carbide/graphite

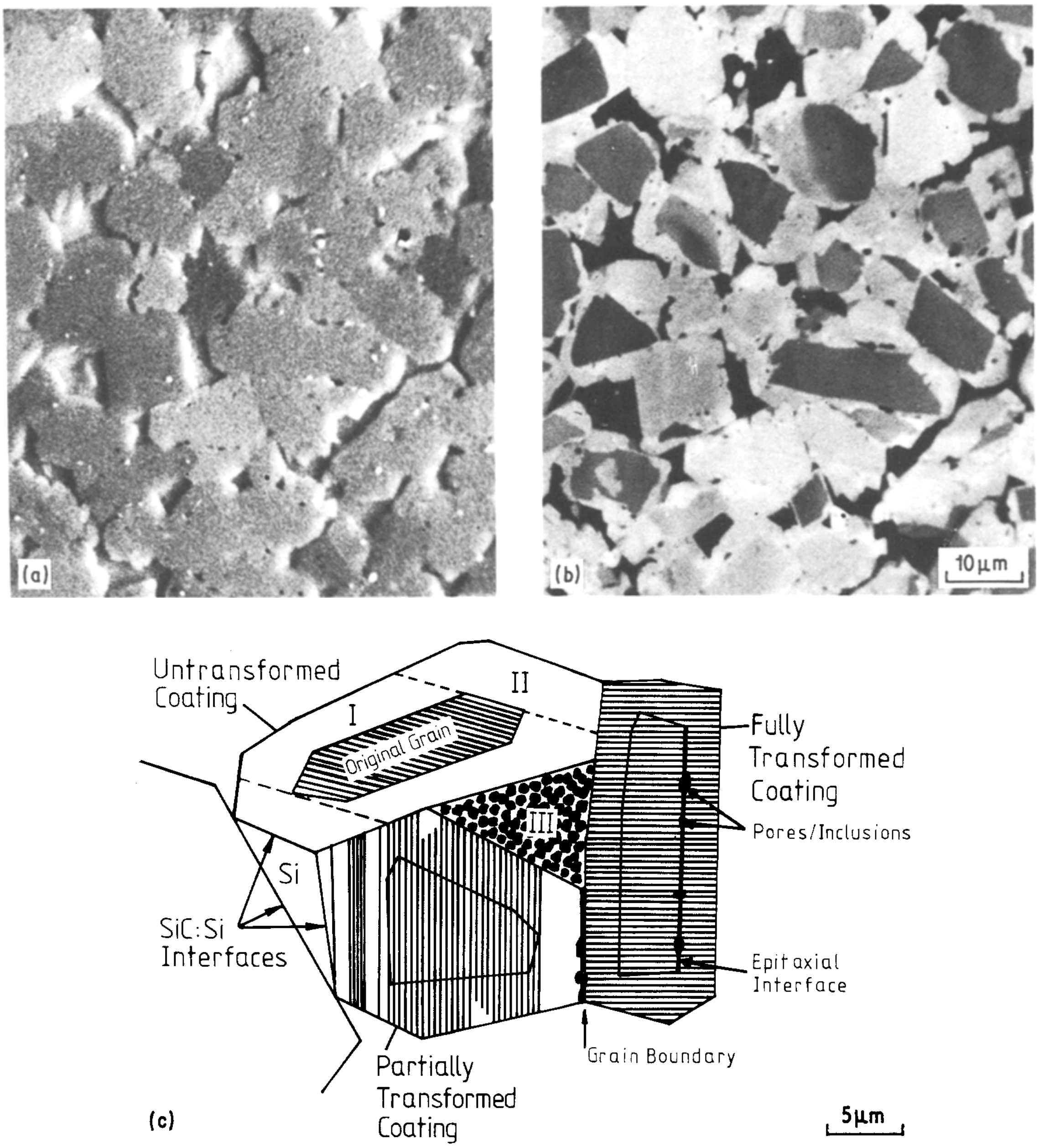

Figure 1 (a) An SEM micrograph of a polished, unetched and uncoated sample of reaction-bonded silicon carbide imaged using 20 kV backscattered electrons. The individual SiC grains are revealed by channelling contrast which shows uniform orientation within any one composite crystal. The residual silicon areas show some polishing relief and appear lighter due to atomic number contrast. Also visible are some small, high atomic number, inclusions decorating both grain boundaries and epitaxial interfaces. (b) As (a), but imaged using secondary electrons, revealing the composite nature of each grain, with different signal levels being controlled by levels of impurity. The original silicon carbide particles usually appear as dark-imaging grain cores, with a lighter imaging epitaxial overlayer. The residual silicon now appears dark. (c) A schematic representation of four grains illustrating various microstructural features and the $\beta \rightarrow \alpha$ transformation occurring in the epitaxial material. The parallel lines represent $\{0001\}_\alpha$ plane stacks. Regions I, II and III represent SiC produced by the Si + C reaction. Regions I and II are epitaxial on the original grain, while region III is the fine-grained material (see Sections 3.2 and 5.1.)

mixture. Addition of a material which is very poorly wet by silicon (such as alumina) can slow down or totally arrest the reaction. On the other hand, if the rise is too rapid the compact can crack due to thermal shock.

The extent to which the graphite will initially dissolve in the silicon is small ($\sim 0.5\%$ [13]), although the presence of certain transition metals is known to increase the solubility (e.g. iron [14]). However, the dissolution is exothermic [13], which causes a local temperature rise at the dissolution sites. This local rise in temperature increases the solubility of the graphite in the silicon causing further dissolution [13]‡. A carbon activity gradient within the silicon is thus produced, causing rapid diffusion away from the sites of dissolution; carbon transport within the silicon is extremely rapid [15] and would not be expected to be a rate-controlling step in the process. The carbon diffuses to locally cooler sites (i.e. the original silicon carbide particles) where it will become supersaturated in the silicon and so precipitate out as "new" silicon carbide. One interesting speculation is that the carbon may diffuse not as isolated atoms, but as C–Si pairs, or even CSi_4 units, implying that the "reaction" may largely occur at the dissolution sites.

Consider the following reactions:

---

‡The measured bulk temperature rise is of the order of several hundred degrees Kelvin.

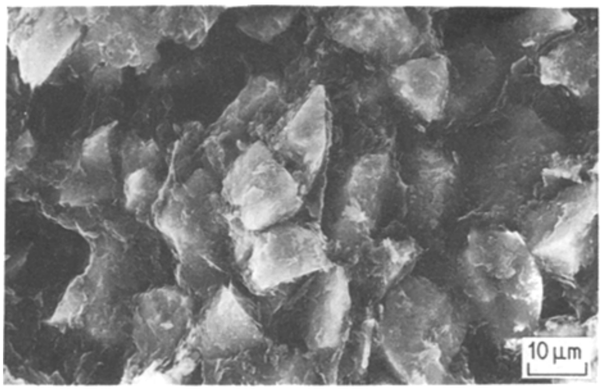

Figure 2 A secondary electron SEM micrograph of a fracture surface of an unreacted compact, showing the original silicon carbide grains covered with colloidal graphite.

$$\mathrm{Si_{(l)} + C_{(graph)} \rightarrow SiC_{(s)}} \quad (1)$$

$$\mathrm{Si_{(l)} + C_{(graph)} \rightarrow Si/C_{(soln)}} \quad (2)$$

$$\mathrm{Si/C_{(soln)} \rightarrow SiC_{(s)}} \quad (3)$$

Thermodynamic data for Reaction 1 show an overall heat of reaction ($\sim 120\,\mathrm{kJ\,mol^{-1}}$ [16]) considerably less than the heat of solution ($\sim 250\,\mathrm{kJ\,mol^{-1}}$ [13]) for the dissolution Reaction 2 (both estimated at a reaction temperature of $\sim 2200°$ C). This implies that the deposition Reaction 3 is endothermic. If this is the case, a large temperature gradient would be produced between the carbon dissolution sites and the nucleation and growth sites (although the precipitation sites will also probably rise in temperature because of the high thermal conductivity of all the materials present). This gradient will allow both rapid dissolution and precipitation to occur, but may be lessened by the good thermal conductivity of the liquid silicon and the silicon carbide. This effect would produce the observed rapid rate of reaction – the process locally takes only a few minutes – as suggested by Sawyer and Page [7].

After most of the new silicon carbide has formed, the exothermic processes will start to decay quite rapidly. Thus any carbon still in solution will rapidly become supersaturated and precipitate out, possibly on any undissolved graphite or even homogeneously. The material so formed is the fine β-SiC that is sometimes found between the grains [6, 7], usually in the large gaps between grains as would be expected (see below).

3.2. Growth morphology

By using rapid quenching to interrupt the bonding process, followed by etching to remove the silicon, we have been able to follow the growth sequence of the new material. Fig. 3 shows a series of SEI micrographs of various stages of the growth process while, in order to facilitate the three-dimensional appreciation of the morphologies involved, Fig. 4 shows stereo-pairs of micrographs also typical of selected stages of the development of the epitaxial coating.

Figs. 3a and 4a show large numbers of small crystals nucleated on each original grit particle and assumed to be epitaxial even at this stage. The distribution of these "nuclei" is uniform and found to be independent of grit size. The nuclei usually appear to be faceted and by the stage of Fig. 3b, not only is this faceting pronounced, but the common orientation of the growths on each original particle is apparent. Using both standard material and the special large-grained specimens, the growth morphology has been determined. A combination of selected-area channelling, serial sectioning and back reflection Laue patterns (see later) have shown this morphology to be consistent with the material forming as β-SiC displaying $\{1\,1\,1\}_\beta$, $\{1\,1\,0\}_\beta$ and $\{1\,0\,0\}_\beta$ facets.

Next, the growing nuclei thicken and begin to coalesce to produce the serrated types of structures shown in both Figs. 3c and 4b.§ Progressive growth and coalescence produce the overlayer morphologies shown in Figs. 3d to f from which the final evolution of a faceted single crystal is evident. The production of such a single crystal growth from a multitude of growth centres confirms the mutual alignment of the original nuclei. Also, the coalescence of different growth centres to form a single uniform growth front often results in re-entrant structures not normally associated with equilibrium single crystal growth. Fig. 4c shows a striking example of the serrated and pseudo-dendritic appearance of the overlayer material. The serrated growth fronts shown in Figs. 3c, 4b and c are produced from the coalescence of parallel $\{1\,1\,1\}_\beta$ sheets, this plane being parallel to the $\{0\,0\,0\,1\}_\alpha$ in the original grain. This suggests growth is most rapid within these planes, probably along $\langle 1\,1\,0\rangle_\beta$ directions. This would confirm the growth morphology suggested by Heuer *et al.* [8]. A possible mechanism of plate broadening is illustrated in Fig. 4b where a large number of parallel finger-like growths can be seen perpendicular to the plates, lying along the other $\langle 1\,1\,0\rangle_\beta$ directions not in the growth plane.

Figs. 3f and 4d show the final microstructure with evidence of both faceted grains and the remains of the serrated structures seen earlier. This leads to the occurrence of both planar and serrated grain boundaries (see Section 4). For comparison, Fig. 5a shows the morphology of β-SiC crystals grown by reacting graphite and silicon in the absence of any original silicon carbide particles. The morphologies and interfacial angles produced are strikingly similar to those shown in Figs. 3e, f and 4d lending further credence to the belief that the epitaxial overlayer grows as the cubic polytype. Fig. 5b shows an example of the fine-scale β-SiC sometimes produced in between the original grit particles. The material is found to be equiaxed and of uniform grain size ($\geq 0.5\,\mu$m). Fig. 5c shows similar fine β-SiC found in one of the nodular structures discussed in Section 5.3. Both examples of fine β-SiC exhibit habits similar to those of Figs. 3f, 4d and 5a. Quenching of a reacting specimen can also produce similar fine material near the reaction zone, but not in already reacted material. No evidence has

---

§Note that the coalescence of the commonly oriented nuclei, together with their morphologies, can often make these structures appear "dendritic" especially when viewed on polished sections (see Figs. 6 and 7).

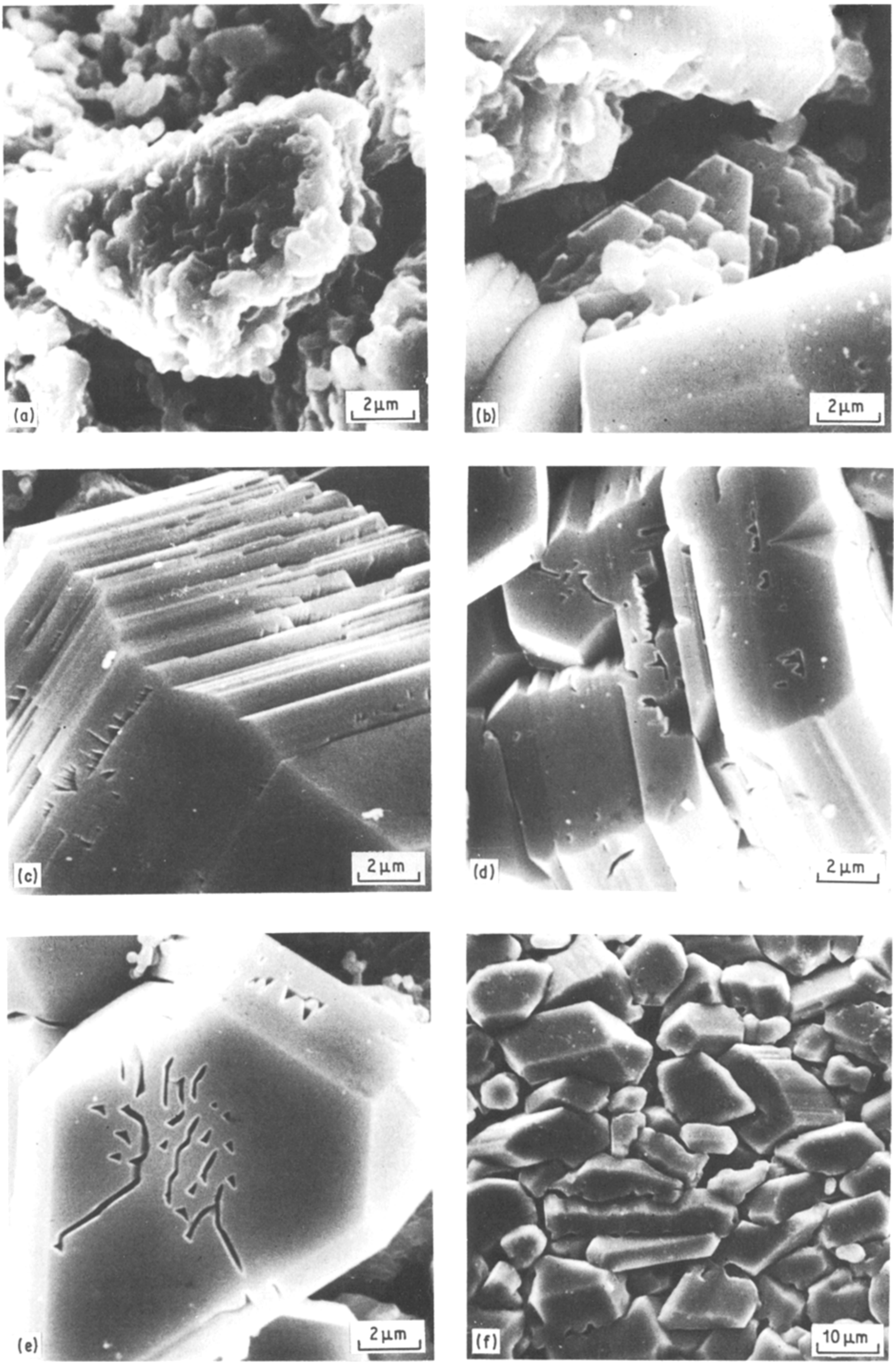

Figure 3 A sequence of secondary electron micrographs illustrating the stages of formation of the epitaxial material, as observed in quenched and etched specimens. Small nuclei initially deposit (a) and then grow outwards as parallel faceted plates (b). These plates then thicken and coalesce, (c) to (e), to form the simple faceted crystals visible in (f), which is taken from fully reacted material (see text).

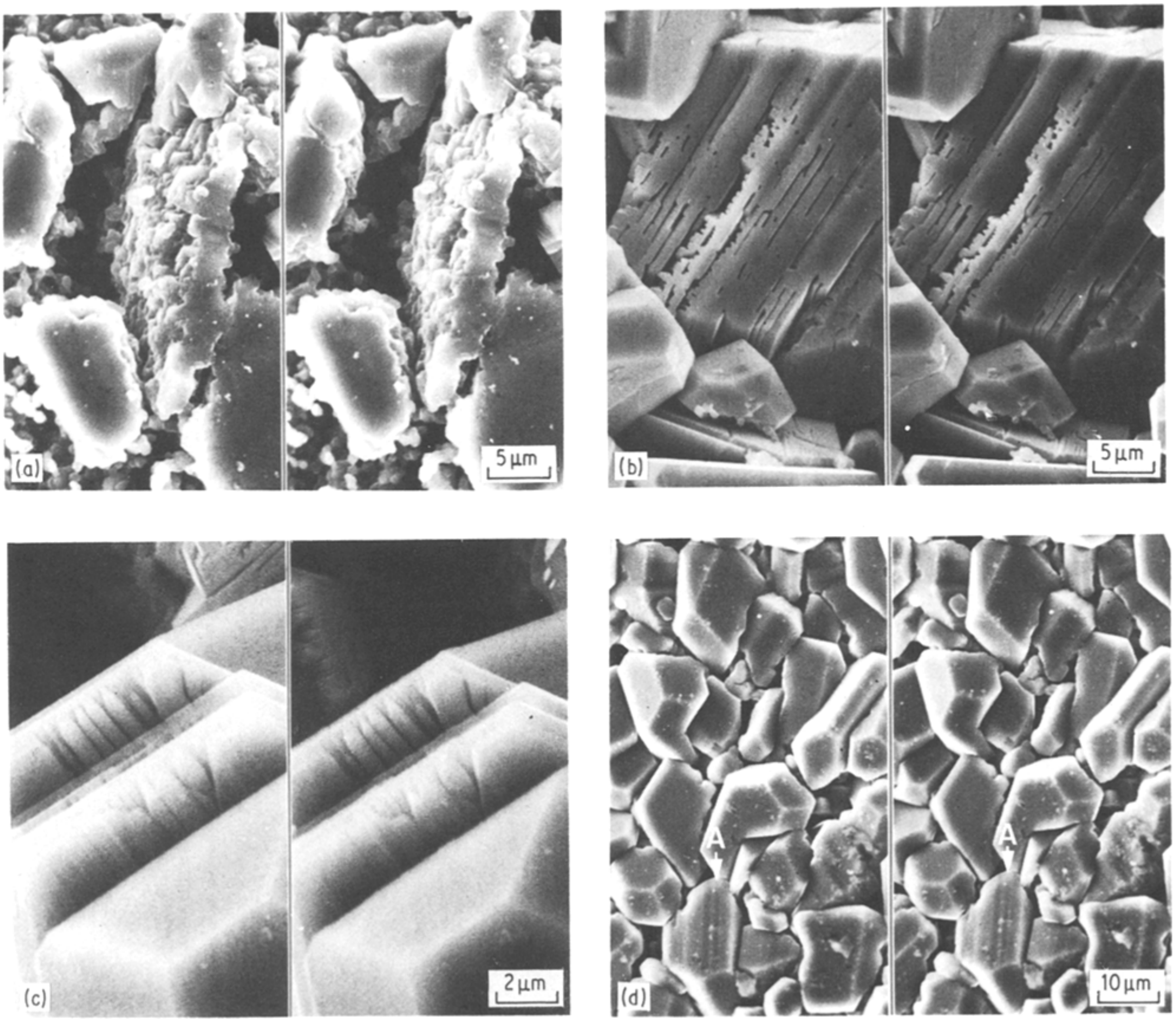

Figure 4 As Fig. 3, but using stereo-pairs to illustrate the morphology of the growing material. The dark stripes in (d) (e.g. "A") represent areas of residual β-SiC, revealed by an intrinsically lower secondary electron coefficient. The morphology of (d) should be compared with Fig. 5a.

ever been found of the fine β-SiC transforming to α-SiC (cf. epitaxial material), which has been explained in terms of this material never experiencing a temperature sufficiently high to cause it to transform [11], as might be expected if it forms during cooling of the local reaction zone.

3.3. The $\beta \rightarrow \alpha$ transformation

We have been unable to determine at what stage of the growth process the $\beta \rightarrow \alpha$ transformation occurs, though reaction kinetics [17] suggest that it only occurs in the very high temperature region very near to the reaction front [11]. Thus, most of the β-SiC growth structures seen in Figs. 3 and 4 may well have already partially transformed to α. That some β remains even in the final microstructure has not only been shown by transmission electron microscopy [9, 11], but is witnessed by the presence of dark striations on some grain surfaces (e.g. at "A" in Fig. 4d), which can be explained as comprising remanent β-SiC material of intrinsically lower secondary electron coefficient than the surrounding α[¶] (e.g. [9, 11]).

Whilst stereo-imaging has enabled the grain morphology of the newly-formed material to be characterized as being consistent with cubic crystallography, this hypothesis being supported by several TEM studies revealing residual β-SiC in partially transformed epitaxial material [9, 11], the specially prepared large-grained samples allowed further confirmation. Fig. 6 shows secondary electron images of polished sections containing large (0 0 0 1)-oriented SiC single crystals in which the growth morphology of the epitaxial material is apparent. Fig. 6a also shows an inset back-reflection Laue photograph from the large crystal. This type of study, combined with similar electron channelling information and serial sectioning has enabled us to confirm that the shapes displayed by the outcrops of "new" material is once again consistent with $\{1\,1\,1\}_\beta$, $\{1\,1\,0\}_\beta$ and $\{1\,0\,0\}_\beta$ bounding facets.

[¶] Note: while some of the striations are topographic in origin, many are seen on flat grain surfaces as assessed by stereo microscopy (cf. Fig. 7).

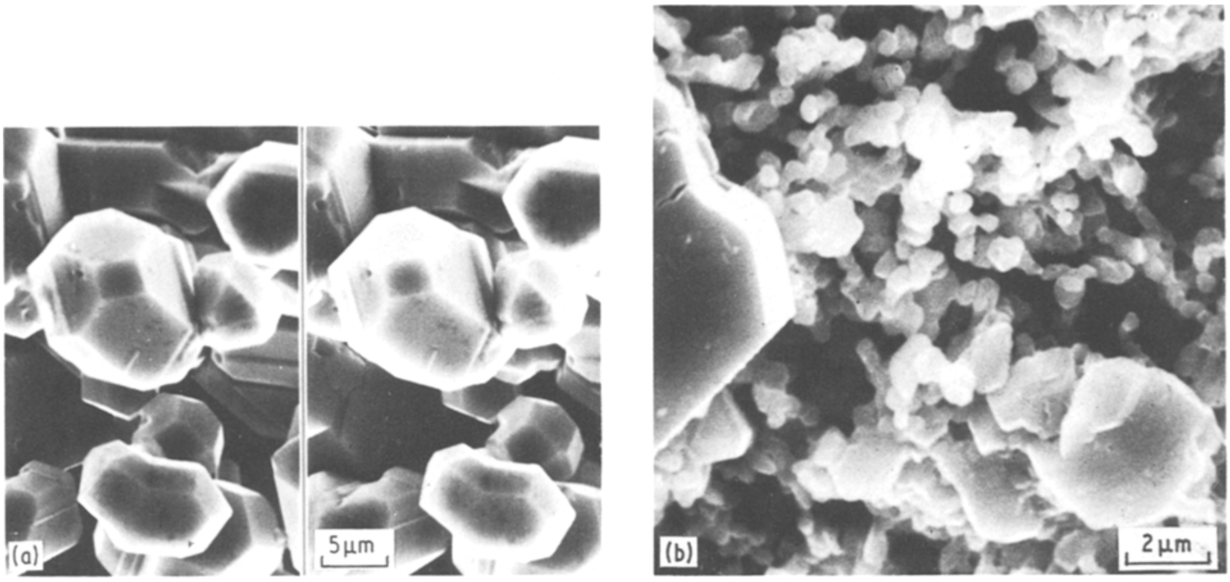

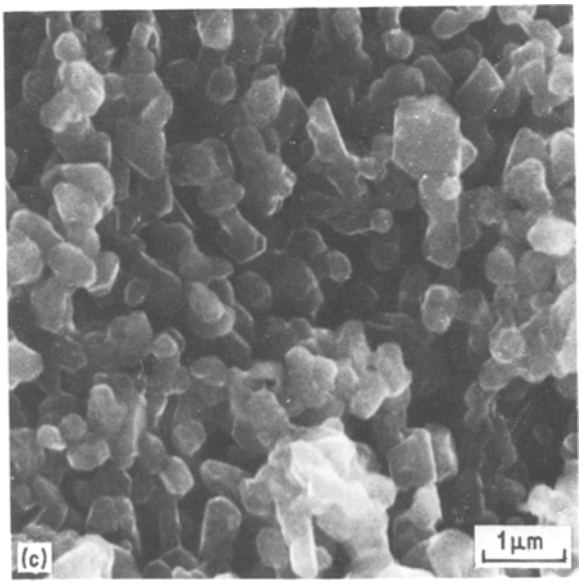

Figure 5 (a) An SEM secondary electron stereo-pair of an etched sample of β-SiC grown by reacting graphite with liquid silicon (cf. Fig. 4d). (see Section 3.2). (b) Intergranular fine-grained β-SiC (SEI) (see Section 3.2). (c) Nodular fine-grained β-SiC (SEI) (see Section 5.3).

3.4. The distribution of impurities

It is interesting to compare the microstructure in different parts of a specimen. As far as the overall grain structure is concerned (i.e. that revealed by etching away the silicon), there is very little basic variation. However, this is not true if polished sections are examined using SEI. Fig. 7 shows three sections through a rod taken from the bottom, middle and top. In each case, representative micrographs from the rod centre and edge are shown. There is a remarkable difference in appearance, in that the section from the bottom of the rod reveals only a very thin light-imaging region in the epitaxial coating. This "sandwich" layer lies between the darker imaging grain core and the rest of the epitaxial layer which also images darkly. The top section shows a very thick sandwich layer, and the middle section a layer of intermediate thickness. As mentioned earlier, Sawyer and Page [7] suggested that the light areas in these images were areas of greater purity ("impure" meaning 100s p.p.m.). However, high spatial and mass resolution secondary ion mass spectrometry (SIMS) [18] and laser ionization mass analysis (LIMA) techniques have revealed the opposite to be the case – the light areas are the impure ones and contain mainly aluminium. This has been confirmed by the relative contrast exhibited by the various large single crystals incorporated into compacts in this study. Those containing aluminium (blue-black) imaged relatively lighter than those with a lower overall impurity level and containing principally nitrogen (green) [19].

This difference in contrast can be explained by considering the impurity solubilities and distributions within the material. Most of the impurities found in the compact are soluble in liquid silicon. Thus, as the silicon rises through the compact is has the effect of concentrating the impurities within itself, i.e. the residual silicon at the top of the billet can be several times as impure as that at the bottom – see Table I [20]. Fig. 8a shows this effect revealed by atomic number contrast in a BEI image of a quenched sample containing a reaction front. However, this concentrating effect is different for different impurities. For those which are soluble in SiC (e.g. Al, N [21]) the effect is only slight; whereas for impurities relatively insoluble in SiC (e.g. Fe, Ca [21]) the effect can be large. Also, SIMS and LIMA studies have shown that the dominant species found in the new SiC is aluminium, which is the most soluble of the available impurities.

These facts suggest an explanation for the observed SEI contrast. As the new silicon carbide forms it is

TABLE I Impurity content of the residual silicon measured at the top and bottom of an extruded specimen, measured for three common impurities

	Impurity level (wt %)		
	Fe	Al	Ca
Top	0.50	0.06	0.04
Bottom	0.16	0.04	0.01

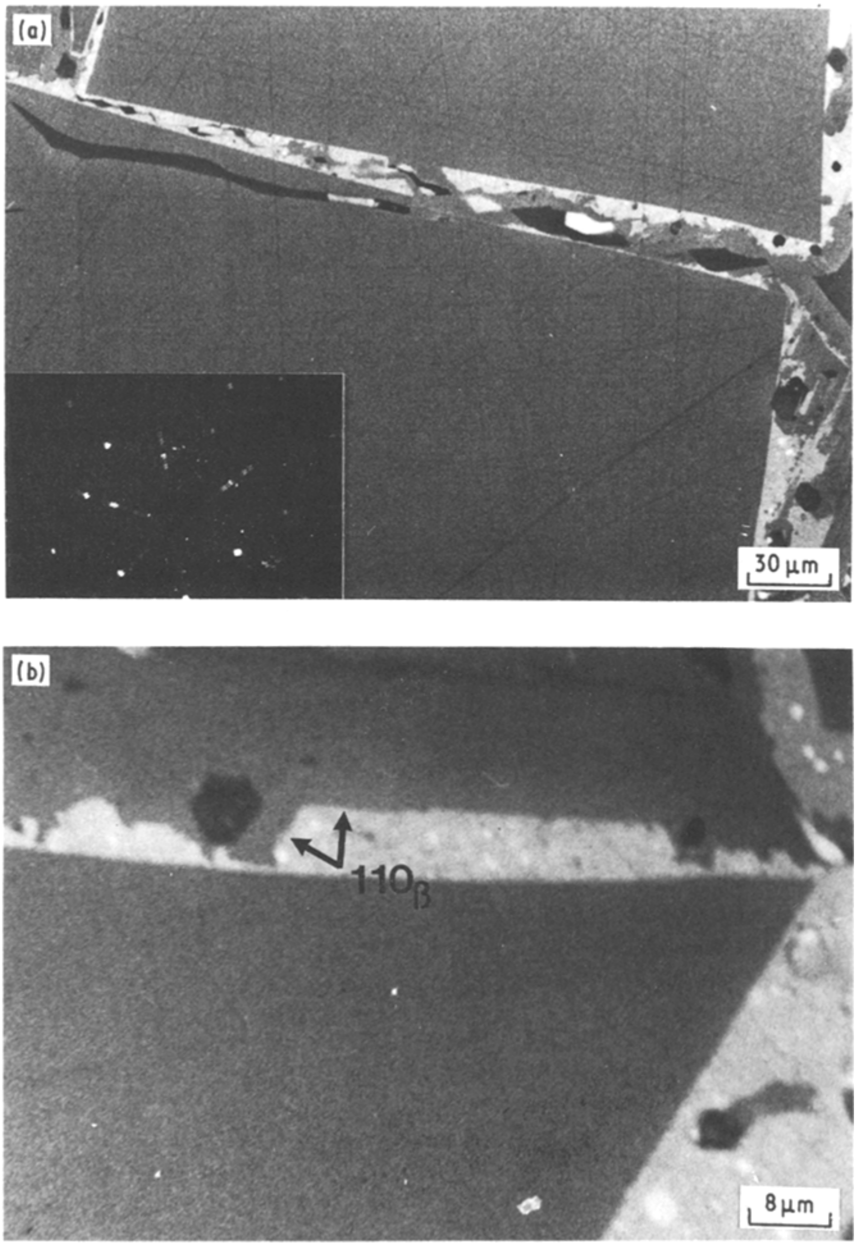

Figure 6 SEM secondary electron micrographs of large (~ 2 mm) single crystals of α-SiC of known (0 0 0 1) orientation (see inset Laue pattern). The new lighter-imaging overgrowths show morphologies consistent with growth as β-SiC. For example, the arrowed faces in Fig. 5b are consistent with both faces being $\{1\,1\,0\}_{\beta}$.

presumed to incorporate some "local equilibrium"* amount of available aluminium.† This incorporation continues until the local aluminium supply from the liquid silicon is exhausted. Beyond this point, the aluminium level in the silicon carbide will rapidly decrease, explaining the apparently sharp light/dark interface observed in the epitaxial material. The thicker light-imaging sandwich layers further up the specimen thus represent larger amounts of available aluminium towards the top of the billet.

One simple consequence of this explanation is that the light/dark interfaces in the epitaxial material represent lines of equal time in the reaction. Thus their morphology would be expected to follow closely that of the etched samples. Comparison of Figs. 3, 4 and 7 shows this to be reasonable, although the exact morphology is not so clear in Fig. 7 because each grain is only a random section. However, serial sectioning shows a good three-dimensional correspondence with etched samples.

If a burn-out layer is present in the material (as it was for the specimen illustrated in Fig. 7) then the silicon flows up the side first and then inwards. This produces a flow pattern similar to the one shown in Figs. 8b, which is a section through a quenched specimen, with the silicon showing light contrast due to its higher average atomic number. Thus, since the silicon is moving both *upwards* and *inwards* through the billet, the argument in the previous paragraph concerning the relative thicknesses of the sandwich layer must be applied with care. For example, points A, B and C in Fig. 8b would all react at the same time and with the same available impurity content in the silicon. Hence, they would all show similar sandwich thicknesses, despite being at different vertical heights in the billet. Thus the "central" section of Fig. 7d has probably

---

*We have been unable to find any data on the partition of Al between SiC and liquid silicon. Furthermore, the non-equilibrium nature of the process would mean that such equilibrium partition coefficients would have to be applied with great care.

†It is possible that the aluminium is being incorporated as AlN, which forms a complete solid solution with SiC [22]; this does not change the basic argument but could possibly mean that the amount of nitrogen available is the limiting factor.

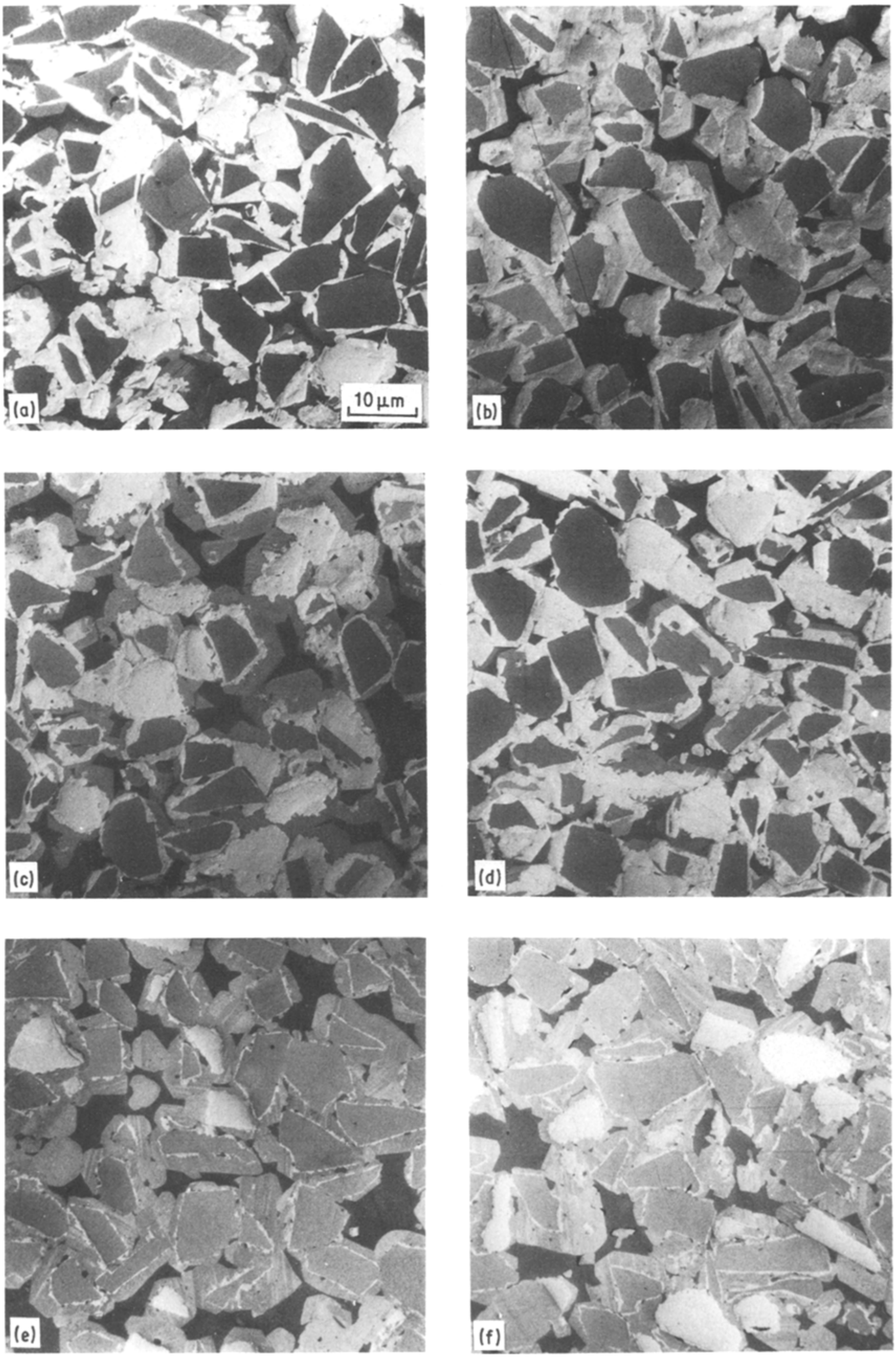

Figure 7 SEM secondary electron micrographs of polished, uncoated and unetched sections from the top (a, b), middle (c, d) and bottom (e, f) of a fully reacted (~ 500 mm × 15 mm rod). (a), (c) and (e) are from the edge of the sections and (b), (d) and (f) from the centre. The increase in thickness of the white "sandwich" layer up the specimen is apparent and corresponds to larger amounts of available impurity (mainly aluminium – see text). Also visible in (e) and (f) are dark stripes corresponding to residual β-SiC.

reacted at a similar time to the "outer" section of Fig. 7a. A consequence of this is that areas near the middle of a section should show a thicker sandwich layer than those near the edge of the same horizontal section. This is indeed found to be the case, as can be clearly seen in Figs. 7c and d.

One final point to notice is the large amount of remanent β-SiC visible in the epitaxial material of Figs. 7e and f, as revealed by the striped regions of darker contrast in SEM images and by bulk X-ray diffraction. This is a consequence of the shorter overall reaction time at the bottom of the billet (due to a

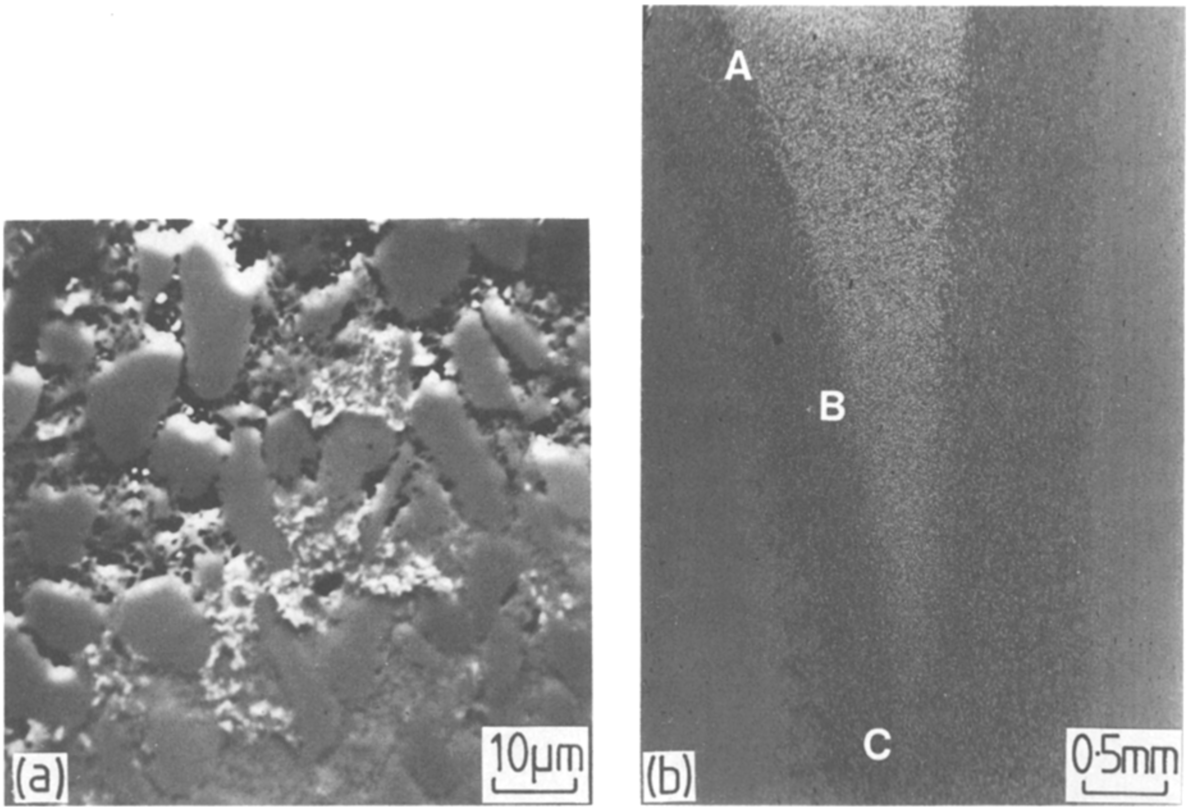

Figure 8 (a) Detail of the reaction zone imaged using backscattered electrons and showing high atomic number impurities concentrated at the reaction front. (b) SEM backscattered electron image of a vertical section through a quenched specimen showing the flow pattern of the silicon. The lighter imaging area corresponds to unreacted silicon, the darker to a partially reacted zone and the grey regions to fully reacted material. The regions marked A, B and C would be expected to show the same thickness of "sandwich" layer (see Fig. 7 and text).

faster rise of the silicon), and a lower overall reaction temperature, meaning that there is insufficient time or energy for the $\beta \rightarrow \alpha$ transformation to go to completion.

4. Grain boundaries

Grain boundaries are formed whenever epitaxial deposits on adjacent grains coalesce. As mentioned in the introduction, the three-dimensional grain-boundary array (e.g. Fig. 9a) is a major factor in controlling the strength of the final material. Thus the precise structure of these boundary regions may be crucial in determining the mechanical properties of the material. High resolution electron microscopy studies of other silicon carbide ceramics have usually revealed a thin wetting layer of amorphous material at SiC:SiC boundaries (e.g. [23]). This layer provides a transition between the directed bond arrays in the surrounding grains, and needs to be a few tetrahedral (~ 0.25 nm) spacings in width to accomodate the mismatch with minimal strain. The thin nature of the boundaries (0.5 to 1.5 nm) necessitates the use of transmission electron optical techniques in their study in order to provide the necessary resolution. However, this has the disadvantage that only a small number of boundaries may be sampled. Various methods have been developed for the study of such narrow regions (e.g. lattice imaging, dark-field imaging) and these have been reviewed in several places (e.g. [24, 25]). Most of these techniques have been applied in this study. However, one problem with silicon carbide is that the principal fringe spacing of 0.25 nm is such that, for most of the microscopes used in this study, optimum fringe visibility occurs at defoci well beyond Scherzer. Even using computed relative fringe shifts from the two grains, this technique still has an uncertainty in the boundary width of about twice the fringe spacing and so has not been used. Therefore, because of its greater accuracy, the principal investigative method has been "defocus" or "Fresnel" imaging as described elsewhere (e.g. [23, 26]).

The most common boundary appearance in REFEL silicon carbide is illustrated in Fig. 9b. In this weakly-diffracting, axial bright-field image, the symmetry of the Fresnel fringes shown by the boundary indicate that it is "edge-on" to the incident beam. Using the approach of Jepps *et al.* [23], the boundary width has been estimated by plotting fringe spacing against defocus; the minimum in this plot being taken to correspond to the boundary width. For all the boundaries measured in this way, the width was found to be 1.05 ± 0.05 nm. This is very similar in width to the boundaries found in Norton NC203 hot-pressed silicon carbide [23], though there is some evidence that the compositions are different (see below).

In general, there is no orientation relationship across the boundaries, although texturing of the material during processing (see Section 7) occasionally produces two grains with a common orientation (e.g. $\langle 10\bar{1}0 \rangle$, $\langle 11\bar{2}0 \rangle$ normal to the boundary. An example of this is shown in Fig. 9c, where it can be seen that there is a certain amount of strain associated with the boundary. The origin of this strain is uncertain but it may arise from thermal contraction on cooling.

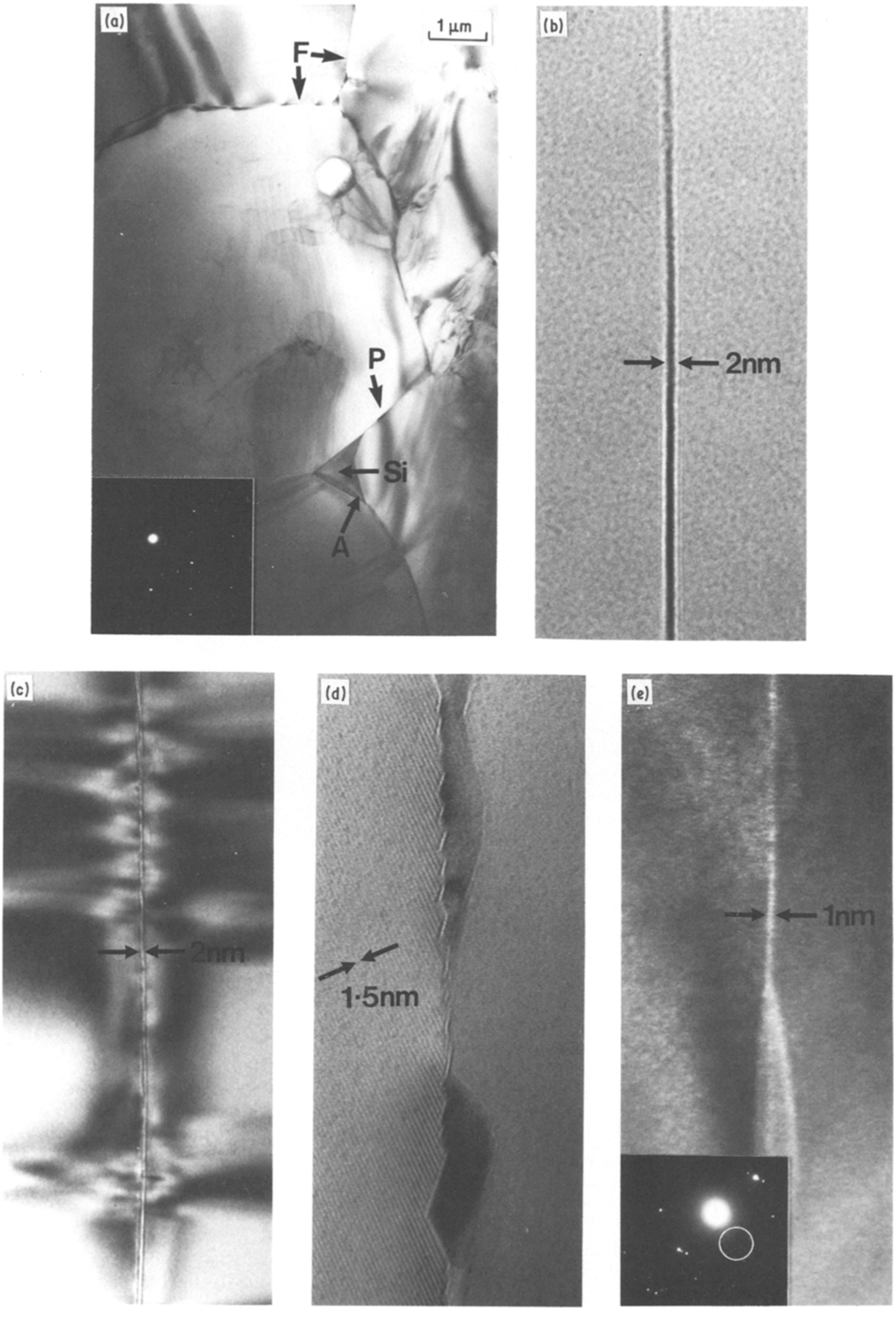

Figure 9 Axial bright-field TEM micrographs of: (a) four grains showing both planar (P) and stepped/faceted (F) grain boundaries; (b) a portion of an "edge-on" boundary displaying symmetrical Fresnel fringes, the variation in fringe spacing with defocus enabling the boundary width to be determined as ~ 1 nm; (c) a similar boundary to (b), showing strain in the material adjacent to the boundary; (d) a stepped boundary showing what were originally $\{1\,1\,1\}_\beta$ and $\{1\,0\,0\}_\beta$ facets, with 1.5 nm $\{0\,0\,0\,1\}_\alpha$ fringes visible in one of the transformed grains; (e) a centred dark-field image of a planar grain boundary, imaged with the aperture in the position shown on the inset diffraction pattern. This position corresponds to a spacing of 0.3 nm (the tetrahedral edge in SiC), suggesting that the boundary consists of amorphous SiC. Also visible is amorphous SiC over the surface of the specimen, caused by ion-beam thinning damage.

The growth morphology of the epitaxial deposit can result in planar, stepped or serrated boundaries, bounded by $\{1\,1\,1\}_\beta$, $\{1\,1\,0\}_\beta$ and $\{1\,0\,0\}_\beta$ facets. Planar boundaries are visible in Figs. 9a to c, although the boundaries only appear edge-on for a few hundred nanometres. This slight deviation from planarity may, however, be partially due to specimen bending during preparation and/or observation. As well as these planar boundaries, stepped and serrated boundaries are produced as a consequence of the serrated growth front mentioned previously. This is illustrated in Figs. 9a and d – the latter boundary showing $\{1\,1\,1\}_\beta$ and $\{1\,0\,0\}_\beta$ facets from one of the grains.

Although these boundaries are of similar width to those found in Norton NC203, their composition seems to be somewhat different. The Norton boundaries probably contain SiO_2 [19, 23], but this composition is unlikely in reaction-bonded material because most of the available oxygen is removed before reaction commences (see Section 6). The boundaries in REFEL silicon carbide seem to contain fairly pure amorphous material. The evidence for this is as follows.

1. Dark-field imaging reveals amorphous haloes from the boundaries lying at positions corresponding to spacings expected of amorphous silicon carbide, specifically 0.19 nm (Si—C bond length) and 0.31 nm (~ tetrahedral side). This is illustrated in Fig. 9e, where the objective aperture has been placed on the amorphous halo corresponding to the Si—C bond length, at 45° to the boundary trace to minimize Fresnel effects. It can also be seen that the boundary phase is continuous (as is always found to be the case). Also visible is the amorphous silicon carbide on the surface of the specimen due to ion-beam thinning damage – this can be used as a calibration for the Si—C bond length.
2. Neither EDS nor EELS analysis in the TEM nor Auger analysis of *in situ* fractured boundaries revealed any detectable impurities (i.e. $\geqq 0.5\%$). The stoichiometry of the boundary film is uncertain (it might be expected that the material would be silicon rich from the bonding process), but Auger measurements indicate a deviation from stoichiometry of less than 1%.
3. Work on matching the intensity (visibility) of the Fresnel fringes at the boundary with computer simulations [26], reveals a drop in the mean inner potential in the boundary, relative to the grains, of only 2 to 4%. This is of the magnitude that would be expected for amorphous silicon carbide since the mean inner potential would be controlled by the relative densities of the amorphous SiC in the boundary and the crystalline SiC in the grains. It is possible to produce a similar result with doping by, say, AlN, but this would be limited to less than 1% by the EDS, Auger and EELS measurements. Most of the aluminium available also appears to be dissolved in the first-formed epitaxial silicon carbide, as outlined in the previous section.

Taking these observations together strongly suggests that the boundary film usually consists of a ~ 1.05 nm wide region of pure, approximately stoichiometric amorphous silicon carbide.

Although the majority of the boundary area in REFEL silicon cabide is of this simple character, most of the boundaries also have pores or inclusions lying along them. This can be seen in Fig. 1 where the inclusions either appear darker (low atomic number/pore) or lighter (higher atomic number) than the surrounding silicon carbide. These inclusions occur even in material made out of very pure starting materials, emphasizing the impurity concentrating effect of the reaction-bonding process. Using a combination of lattice imaging, selected-area diffraction and EDS, these inclusions have been fully characterized and can be classified into three types:

1. Those containing residual graphite (Fig. 10a). This graphite remains because it is trapped by the growing grains before it can be dissolved in the silicon and hence reacted.
2. Those containing residual impure silicon.
3. Those containing various silicides. When the solubility of the impurities in silicon is exceeded on cooling, silicides are produced. Fig. 10b shows a lattice image of Ca_2Si showing 0.48 nm fringes. The silicides found are almost exclusively those of iron, calcium and titanium.

The residual graphite and silicon probably have little effect on the mechanical properties of REFEL silicon carbide below the silicon melting temperature. However, several of the silicides have relatively low melting points and, on melting, can produce porosity which may seriously weaken the material [19, 20].

5. Other microstructural features

5.1. SiC:SiC epitaxial interfaces

These are the nominally perfect interfaces between the "old" and "new" silicon carbide. In general, the $\beta \rightarrow \alpha$ transformation that occurs in the epitaxial deposit (shown schematically in Fig. 1c) is "seeded" at these interfaces by the stacking sequence in the original crystal. Thus, the new material transforms from β to the particular α polytype of the seed (e.g. region I in Fig. 1c). However, those portions of the interface parallel to $(0\;0\;0\;1)_\alpha$, that is those where the interface does not intersect the original particle stacking sequence (e.g. region II in Fig. 1c), may transform to a variety of other α polytypes [11].

The epitaxial interfaces are "visible" in SEM images either as a boundary between a dark grain core and white epitaxial material or as a dark line between a white grain core and white epitaxial material, the line being due to topographic contrast caused by differential polishing (e.g. Fig. 7). Also usually present are lines of inclusions [7] along the interface, which are the same in form as those found along grain boundaries. These lines of pores provide a convenient way of locating the interfaces in TEM specimens. Most 6H/6H interfaces (by far the most common) seem to be fully coherent [9, 11], with only occasional strain and misfit (e.g. Fig. 11a). Bearing in mind that the new material originally deposited as 3C, this good matching reflects the similar molar volumes of 3C and 6H [17]. In the case of seed crystals of 4H and 15R (the two next most common polytypes), however, this is

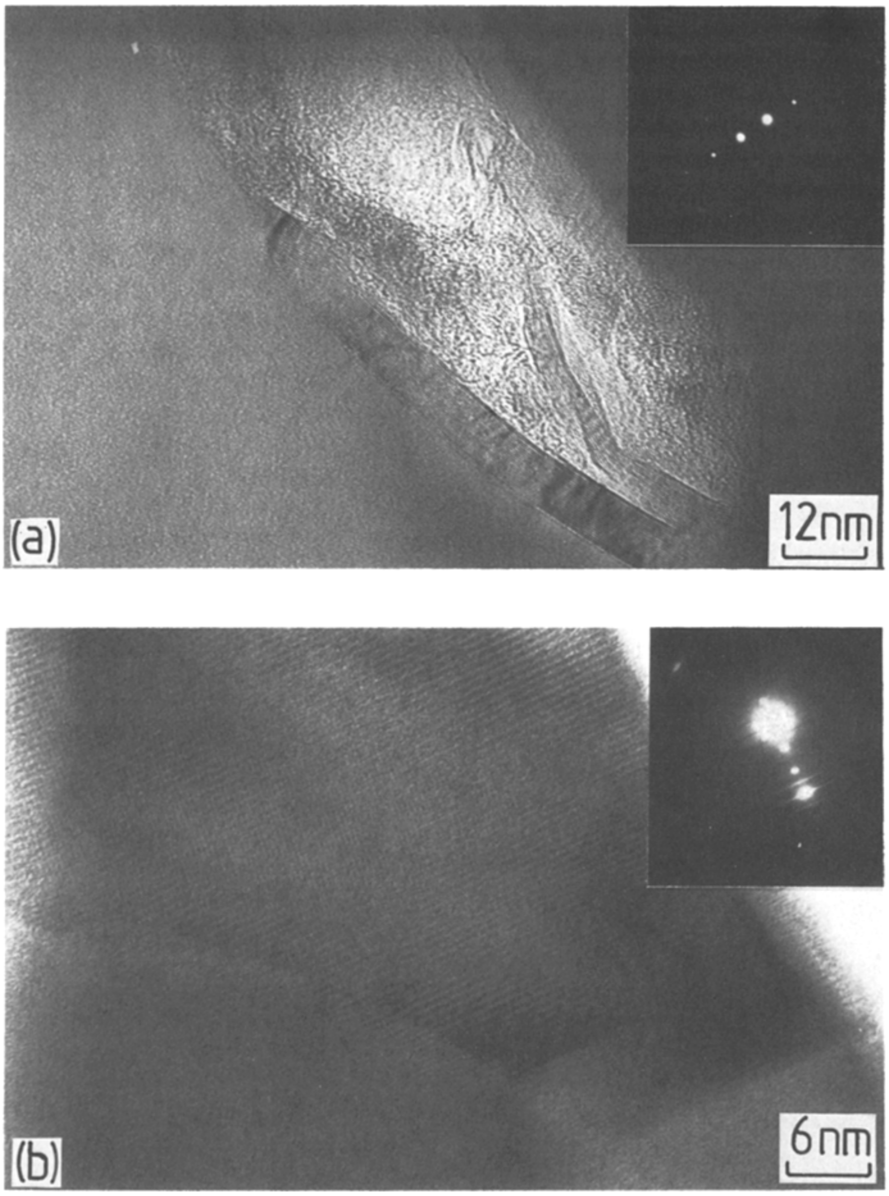

Figure 10 Axial bright-field lattice images of (a) graphite and (b) calcium silicide inclusions found in pores lying along both grain boundaries and epitaxial interfaces.

not the case. Both have a molar volume about 1% less than that of 3C and invariably seem to produce mismatched and strained interfaces [11]. An example of such an interface in a polytype based on 4H (in fact 111R) is shown in Fig. 11b, which has a large amount of local strain associated with it. Where there is no visible strain the mismatch seems to be taken up by partial dislocations (e.g. "A" in Fig. 11b).

Despite these defects the boundaries appear to be very strong since fracture almost never occurs along them.

5.2. SiC:Si interfaces

These interfaces are formed between the solidifying residual silicon and the newly formed silicon carbide (either the epitaxial coating or the independently nucleated fine β-SiC, if present), and are probably the nucleation sites for silicon solidification. Generally they are mechanically weak which is witnessed by their being the preferential paths for indentation fracture [2, 27, 28] and also the first sites where polishing damage becomes apparent as shown in Fig. 12a. Despite their importance in controlling mechanical properties, very little is known about their chemical or structural nature. Fig. 12b shows an axial bright-field HREM image of part of such an interface from a region including some untransformed β-SiC. The matching of the inclined $(1\,1\,1)_{\mathrm{Si}}$ and $(1\,1\,1)_{\beta\text{-SiC}}$ plane stacks suggest that a specific orientation relationship is present, the orientation of the interfacial plane ensuring almost complete registry of the planar spacings resolved along the interface (e.g. [29]). This relationship is the same as that expected from the respective crystal structures (i.e. $(2\,2\,2)_{\mathrm{Si}} \| (2\,2\,0)_{\beta\text{-SiC}}$ since $d^{\mathrm{Si}}_{222} \sim d^{\mathrm{SiC}}_{220} \sim 0.154\,\mathrm{nm}$). For the 6H-SiC:Si interface a similar match occurs for half of each unit cell (i.e. at least for those portions of the 6H stacking sequence in registry with the untransformed β-SiC). There is also evidence of misfit dislocations and interfacial steps (see "A" and "B" in Fig. 12b). Thus, the polycrystalline nature of the residual silicon is probably determined by the occurrence of such crystallographically controlled nucleation sites.

At other parts of the interface, image contrast with varying defocus suggests some evidence for the presence of a thin amorphous film of (as yet) undetermined composition. This film could well dominate the mechanical properties of the interface and further work is proceeding in this area.

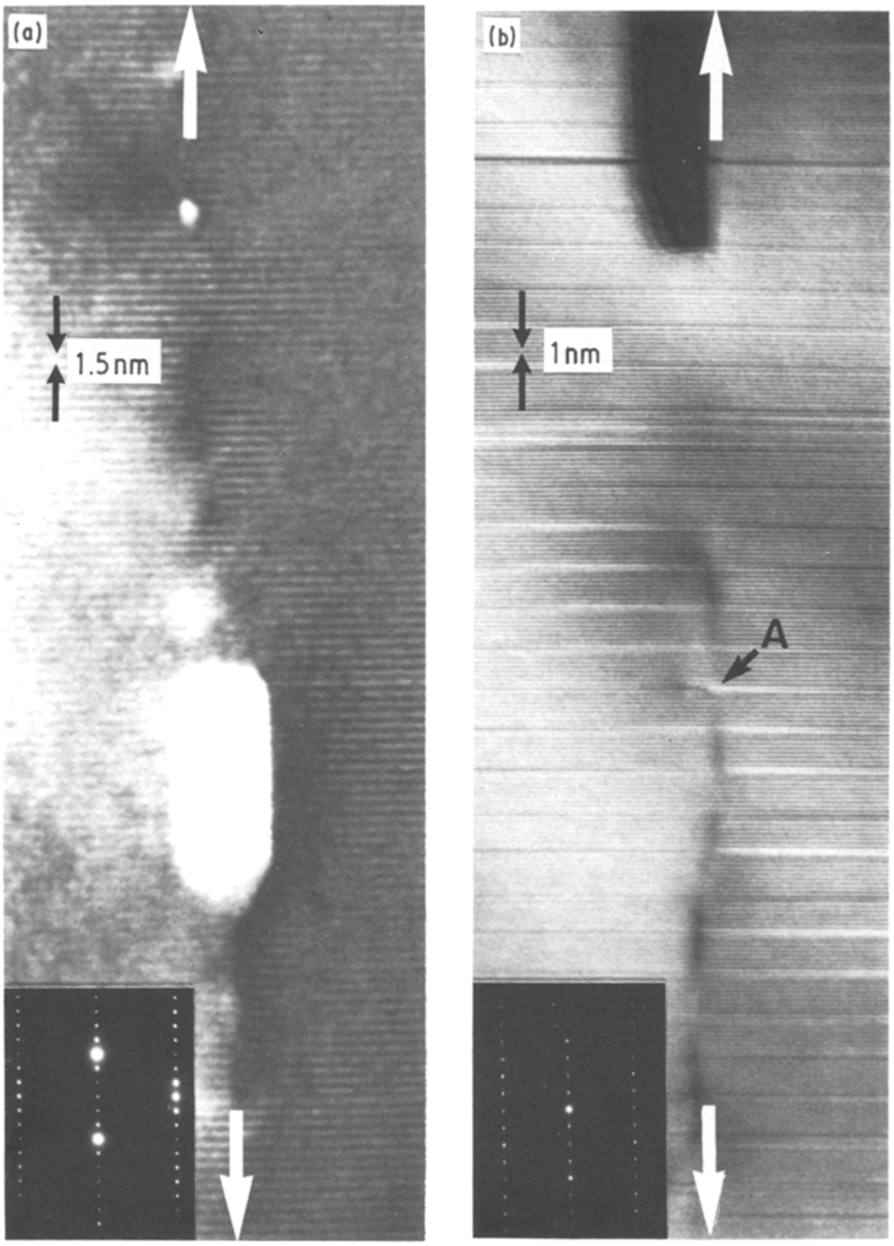

Figure 11 Axial bright-field lattice images of epitaxial interfaces (arrowed) in (a) 6H and (b) 111R grains. Visible in both images are pores and inclusions delineating the interface. The 6H interface is largely perfect, whilst the 111R interface shows both strain and misfit dislocations (e.g. "A") (see text).

5.3. Macrodefects: "nodules" and "Si-cracks"

As mentioned by Sawyer and Page [7], poor mixing in the compact can lead to the formation of regions containing little or no initial silicon carbide. During reaction, the absence of original grit surfaces as nucleation sites produces large amounts of, mainly, fine β-SiC. Three types of such nodules have been identified.

1. Areas of unreacted graphite, surrounded by a layer of fine β-SiC and/or silicon (e.g. Fig. 13a).
2. Areas of mainly fine ($\leqq 0.5\,\mu$m) β-SiC, either of uniform or varying grain size, and residual silicon. The β-SiC is equiaxed and this is the most common sort of nodule (e.g. Figs. 13b and 4c).
3. A nodule containing a central core of β-SiC surrounded by a region of 2H-SiC/β-SiC/Si (e.g. Fig. 13c and see [11]).

Many nodules also contain silicides and impurity-rich regions. These nodules would be expected to contribute little or nothing to the final strength, and may even act as fracture initiation sites. However, they can can be eliminated by good compact mixing.

As mentioned in the experimental section, cracking of the compact prior to silicon infiltration results in silicon-filled cracks occurring in the final compact. These are also mechanically weak, but again can be eliminated by careful processing.

6. Impurities

The impurity redistribution during the reaction-bonding process has been mentioned in several sections already. However, impurities are so important in controlling both the process and the material's final properties that it seems worthwhile to describe the source, movement and final distribution of impurities in more detail.

The original silicon carbide is almost always green-coloured Acheson grit, which has nitrogen as a dominant impurity [e.g. 30] – it is these grains that produce the dark grain cores in secondary electron images. The occasional white grain cores are explained by the presence of material having a large amount of

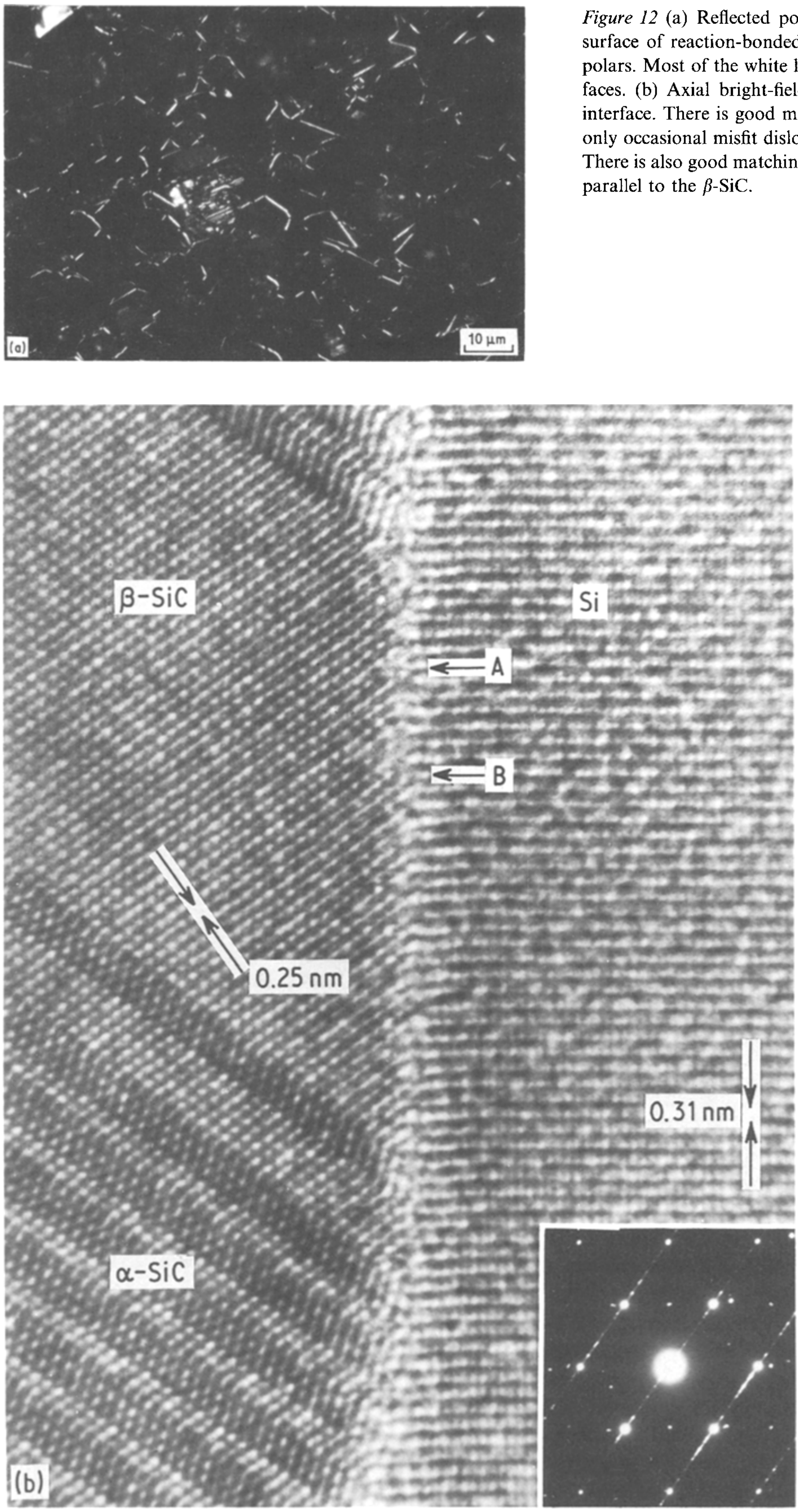

Figure 12 (a) Reflected polarized light micrograph of a polished surface of reaction-bonded silicon carbide taken through crossed polars. Most of the white lines correspond to broken SiC:Si interfaces. (b) Axial bright-field HREM structure image of a SiC:Si interface. There is good matching between the Si and β-SiC, with only occasional misfit dislocations (e.g. "A") and steps (e.g. "B"). There is also good matching between those parts of the α-SiC stack parallel to the β-SiC.

aluminium in solution as well, and appearing blue-black in colour [e.g. 30]. The grits also have a thin SiO_2 coating. Older batches of material were prepared from transistor-grade silicon, but now fairly impure silicon is often used, containing $\leq 1\%$ of elemental impurities, chiefly iron, aluminium, nitrogen, calcium and titanium (see Table II in Sawyer and Page [7]). One final source of impurity is the mixing process itself, where the abrasive action of the silicon carbide on the mixing vessel adds a significant amount of iron to the mix.

These original impurities are redistributed to a large extent during the bonding process, as follows.

1. Before the C + Si reaction commences, some of the impurities are vaporized from the compact,

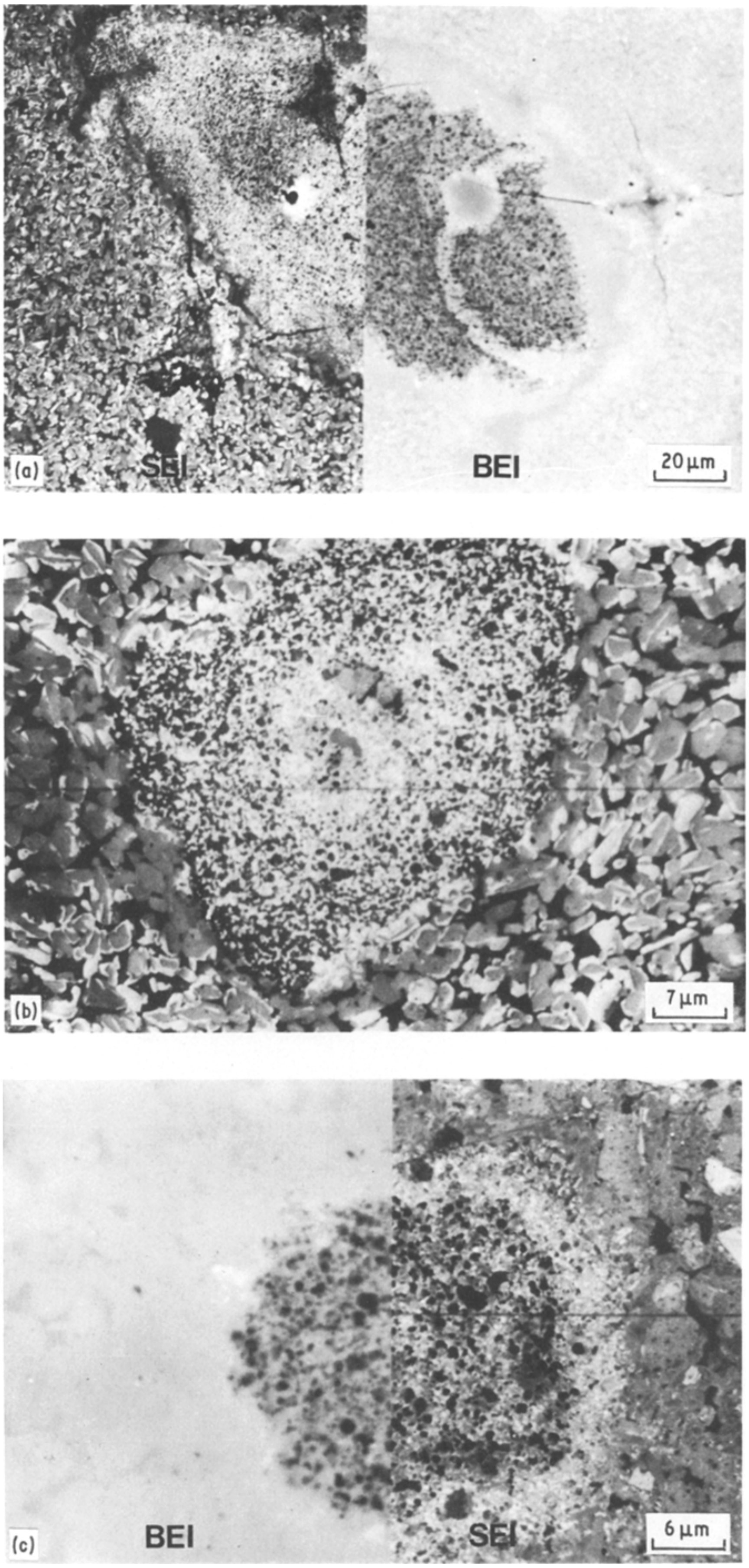

Figure 13 SEM micrographs of nodular structures in polished, uncoated sections. (a) SEI/BEI split-image of a nodule of unreacted graphite surrounded by a layer of fine β-SiC. The three microhardness impressions were made to investigate any preferred indentation fracture paths in these areas. (b) SEI image of a nodule of fine β-SiC. (c) BEI/SEI split-image of a nodule of β-SiC, surrounded by a region of 2H-SiC/β–SiC/Si.

TABLE II Modulus of rupture (MOR) in three-point bending for extruded specimens measured with specimens cut both along and perpendicular to the extrusion direction. Mean linear intercept lengths (MLIs) for both the grain cores and whole grains are also given as are the inverse square roots of these same lengths. A reasonable fit to $\mathrm{MOR_E} \propto (\mathrm{MLI_R})^{-1/2}$ and $\mathrm{MOR_R} \propto (\mathrm{MLI_E})^{-1/2}$ is apparent (see text).

	MOR (MPa)	MLI* (μm)		$(\mathrm{MLI})^{-1/2*}$ ($\mu\mathrm{m}^{-1/2}$)	
		Cores	Grains	Cores	Grains
Extrusion (E)	431 ± 10	12.8	16.0	0.28	0.25
Radial (R)	321 ± 15	7.20	11.0	0.37	0.30
Ratio	1.34	1.78	1.46	0.76 ($=1.32^{-1}$)	0.83 ($=1.20^{-1}$)

*Porportional to flaw size perpendicular to length.

forming a deposit on cooler parts of the furnace. At this stage, the silica coating on the grits is removed by reaction with the carbon.

2. As the silicon sweeps up the specimen it carries impurities from the carbon and silicon along with it, concentrating them as it progresses. This was illustrated in Fig. 8. When the fully reacted compact is cooled, the silicon expands and is squeezed out onto the surface of the specimen to form small "blobs", which are usually removed by grit blasting. These "blobs" also contain a high level of impurities, largely silicide phases, since most impurities are almost insoluble in solid silicon.

3. The distribution of impurities within the newly-formed silicon carbide is controlled by the relative solubility of impurities (e.g. aluminium, boron and nitrogen are orders of magnitude more soluble that iron, calcium, titanium, etc. [21]) and their availability. Aluminium (and possibly nitrogen) seems to be incorporated into the newly formed silicon carbide at a certain level (governed by either the maximum solubility or partition with the silicon) until the supply is exhausted, whilst most of the other impurities seem to be rejected. The position in the specimen determines the amount of aluminium available in the manner explained in Section 3 and in turn, this controls the "sandwich" contrast in secondary electron images.

4. Various small inclusions are found lying along the epitaxial interfaces and the grain boundaries. These contain residual silicon and other material that has been trapped by the growing silicon carbide, such as residual graphite and various silicides. There is no evidence of any impurity segregation to the thin grain-boundary regions.

7. Anisotropy

Anisotropy may occur in materials for a variety of reasons, such as texturing by slip, preferential growth of new material and/or mechanical particle alignment. It is the last of these that is the source of the anisotropy found in REFEL silicon carbide. The α-SiC grits that are normally used are non-equiaxed due to preferential cleavage on $\{10\bar{1}0\}_\alpha$ and $\{11\bar{2}0\}_\alpha$ with secondary cleavage on $\{0001\}_\alpha$. *In extremis*, tabular grains may even be formed.[‡] β-SiC grit tends to be equiaxed with $\{111\}$, $\{110\}$ and $\{100\}$ facets.

Two different forming routes, extrusion and pressing, were considered in this work. The anisotropy was studied using quantitative microscopy to determine the mean linear grain intercept in a particular direction in a particular section. Polar diagrams of mean linear intercept as a function of angle were thus produced. Three cases were examined.

1. Extrusion of α-SiC. Fig. 14a shows a polar plot for both the cores and final grains in a longitudinal billet section containing the extrusion direction. The section exhibits considerable anisotropy, this being greater (as a ratio) for the cores than for the final grains. It is also apparent that, on average, a fairly uniform amount of epitaxial material has been deposited around the cores. This plot is consistent with nominally flat particles aligned edge-on along the extrusion direction.

Table II shows modulus of rupture (MOR) data [20] for three-point bend specimens cut with their lengths parallel and perpendicular to the extrusion direction. Alongside this are the mean linear intercepts, measured from Fig. 14a, for the same two principal directions. The intercepts and their square roots are shown for both the grain cores and the final grains. The different proportional decreases in the mean linear intercept measurements between grains and cores reflects the fairly uniform thickness of the epitaxial coating. Furthermore, the ratio of the MOR values in the principal directions are remarkably similar to the inverse ratios of the square roots of the grain sizes also in the principal directions (i.e. $\mathrm{MOR} \propto d^{-1/2}$).[§] However, since the fracture-initiating flaws are SiC:Si interfaces, it may be that the silicon distribution, and hence the SiC:Si interface distribution, is itself controlled by the grain alignment. Thus it is the anisotropy of the silicon regions between the aligned grains which seems to explain the anisotropy in the MOR data. This is confirmed by Fig. 14b, which shows surface roughness traces both parallel and perpendicular to the extrusion direction in the polished section used to generate Fig. 14a. Although the average height (R_a) of the measured features is very similar, the average spacing between the features is very different. In fact, the relative spacings have a ratio of about two, which is similar to the grain size

---

[‡] Note that while the growth morphology of α-SiC is usually $\{0001\}$ plates, $\{10\bar{1}0\}$ and $\{11\bar{2}0\}$ cleavage may produce tabular grains not of $\{0001\}$ habit. This variation of habit, together with the superposition of many common X-ray reflections (e.g. $\{0006\}_{6H}$, $\{10\bar{1}2\}_{6H}$), is the reason for using polar linear intercept diagrams rather than X-ray pole figures. In fact, the investigation of the growth morphology of the epitaxial SiC has enabled us to recognize non-$\{0001\}_\alpha$ plate-like morphologies.

[§] Since the flaws critical in controlling fracture will mainly be those perpendicular to the length of the MOR specimen, the ratios are as expected i.e. $\mathrm{MOR_E} \propto (\mathrm{MLI_R})^{-1/2}$ and $\mathrm{MOR_R} \propto (\mathrm{MLI_E})^{-1/2}$, where E and R represent the extrusion and radial directions, respectively.

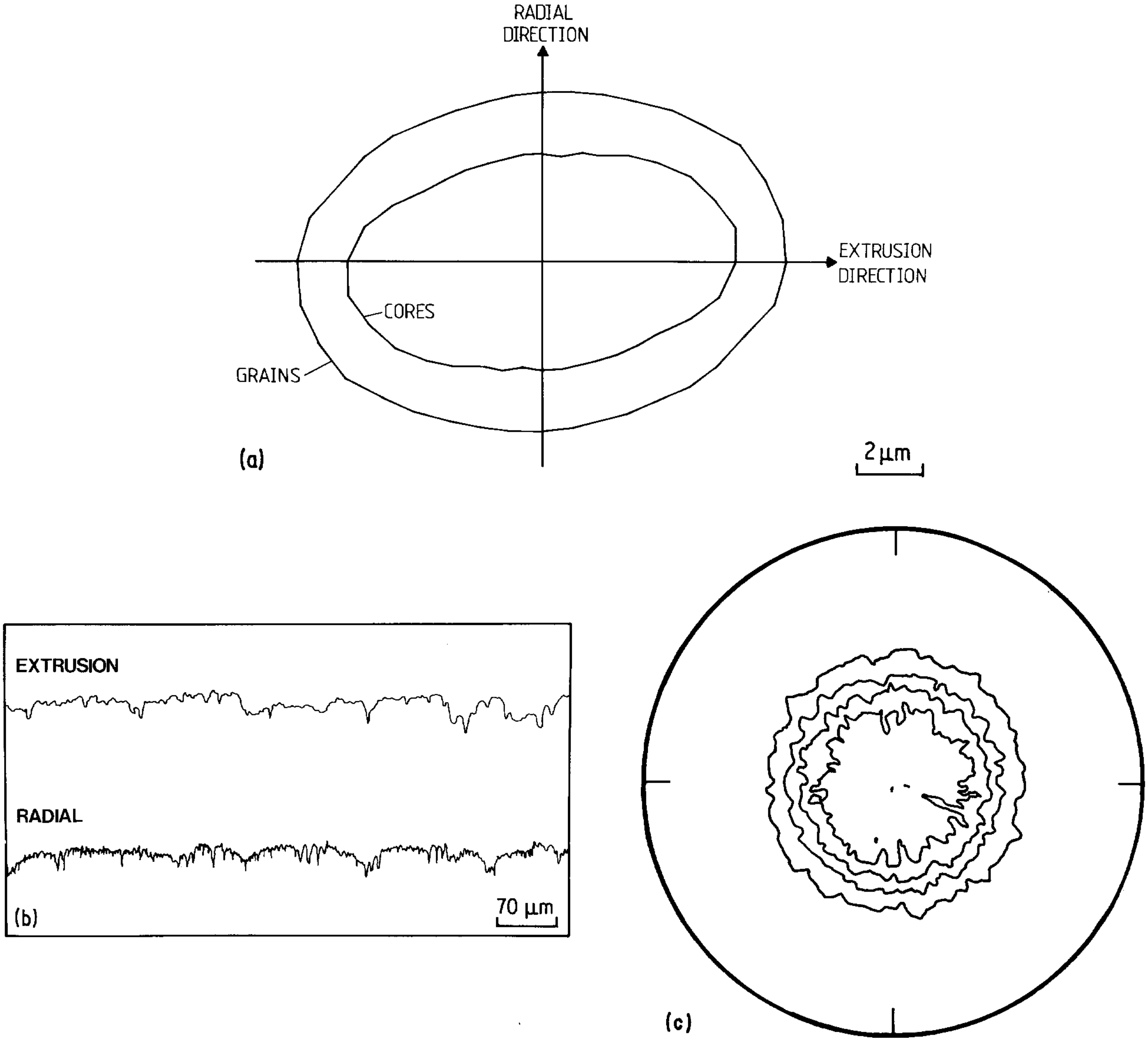

Figure 14 (a) A plot of mean linear intercept against direction for the grains and cores in a section of an extruded specimen, the section containing the extrusion direction. (b) "Talysurf" traces in the principal directions of the specimen used to generate (a). (c) $\{1\,1\,1\}_\beta$ X-ray texture pole figure of a polished section of pressed β-REFEL silicon carbide, taken in the plane of pressing.

ratio in Fig. 14a and Table II. Since it is the preferential polishing of the silicon which produces the features on the trace, this demonstrates that the size of the regions of residual silicon are controlled by the grain alignment of the silicon carbide. Thus these surface measurements confirm the origin of the bend test anisotropy.

2. Pressing of α-SiC. Pressed samples produced very similar plots to those of the extruded material, but with a more pronounced isotropic section being produced perpendicular to the pressing direction.

3. Pressing of β-SiC. No shape anisotropy was detected for this material, as might be expected. However, the $\{1\,1\,1\}_\beta$ X-ray texture pole figure shown in Fig. 14c shows a marked anisotropy with $\{1\,1\,1\}_\beta$ plane normals centred about the pressing direction. This seems to indicate that the β-SiC likes to sit on $\{1\,1\,1\}$ – possibly because these are the largest faces. This anisotropy would be expected to have little effect on mechanical properties.

8. Discussion

Several points have already been discussed in earlier sections, but a number of issues require further elaboration. These are now presented.

8.1. The reaction

The basic reaction mechanism was outlined in Section 3.1 and from this description it is clear that the reaction occurs in a very localized manner (i.e. on a scale $\leq 10\,\mu$m), as suggested elsewhere [4, 7]. The local nature helps to explain the rapid rate of reaction, with its attendant large rise in temperature, but the detailed heat flow in the reaction zone is still unclear. Without any resultant temperature gradient between dissolution and precipitation sites, it seems unlikely that the rapid reaction rate would be observed, since the graphite would be more likely to remain in solution. The reaction time would seem to be too brief to allow convective effects to become important.

Since carbon transport in liquid silicon is extremely rapid, the actual rate-determining step in the process seems to be either the precipitation or dissolution steps. The actual mode of carbon transport (e.g. as C, C–Si, CSi_4) would be important in determining where the "reaction" actually occurs. Thus it is possible that carbon diffusion occurs as CSi_4 (or SiC_4) tetrahedral units, and that it is these units which subsequently precipitate out. Clearly, there is very little bulk transport of carbon beyond a range of about 10 μm. However, the very low solubility of the carbon in the silicon suggests that the dissolution process is rate-controlling. This is supported by the observation that nucleation and growth appear to be relatively easy.

Although the local temperature distribution is uncertain, the bulk temperature rise at the reaction front has been shown to be be sufficient to promote the $\beta \rightarrow \alpha$ transformation. Since the reaction locally takes ~4 min, known kinetic data then suggest a peak local temperature of ~2000° C in the epitaxial material [11]. However, the exact timing of the $\beta \rightarrow \alpha$ transformation, relative to the growth of the epitaxial β, is still unknown. Interestingly, the fine β-SiC never transforms. This is presumably because it does not experience this peak temperature during its precipitation from liquid silicon, which implies that it forms as the material behind the reaction front cools back to the nominal bonding temperature [11].

8.2. Growth morphology

The formation of the epitaxial material is a nucleation and growth process which seems to be independent of original grit size (10 μm upwards). Each original SiC particle seems to provide a large number of equally spaced nucleation sites (Figs. 3a and 4b). It is possible that the nuclei form on $\{0001\}_\alpha$ terraces or ledges on the surface of the original grit particles. This might help to explain their initial preference for a single plate-like $\{111\}_\beta$ growth habit (e.g. Fig. 3b). The etching away of the silicon illustrates this and also helps to confirm that $\langle 110\rangle_\beta$ is the preferred growth direction. The final coalescence of two growing grains produces the SiC:SiC grain boundaries, the occasional "serrated" or "stepped" grain being explained by a serrated growth front of one of the grains.

8.3. Impurities

Although there is no large-scale carbon diffusion, the silicon acts as a solvent for the large-scale transport of impurities insoluble in SiC. Those that are not trapped in the compact are concentrated towards the top, partially in the silicon "blobs" that are squeezed out on to the surface. Combining this observation with the observed removal of silica (by reaction with carbon) from the surfaces of the original SiC, highlights a remarkable self-cleaning process which finally produces grains bonded together by clean grain boundary films of ~1 nm thick amorphous SiC. By comparison, most of the soluble impurities (e.g. aluminium, nitrogen, are incorporated into the early-formed silicon carbide.

8.4. Secondary electron contrast

In contrast to the suggestion of Sawyer and Page [7], microanalytical techniques have shown that the lighter-imaging SiC areas in secondary electron micrographs are relatively impure, largely containing aluminium ($\leq 1\%$ maximum solubility). Since aluminium is an acceptor in SiC, this suggests that secondary electron supply is more important than escape in controlling the secondary yield (e.g. [31]). It is possible that the similar contrast reported in cubic BN [32] may be explained likewise. Also apparent is the intrinsic difference in secondary yield between α and β of the same nominal composition (the dark bands in the epitaxial material are β-SiC) which is explained by a difference in band gap. Our results confirm that these contrast effects are important in enabling good resolution (i.e. typically that of the SEI in the SEM) of small impurity and structural differences and hence allow the microstructure to be more easily elucidated.

8.5 Interfaces

The grain boundaries are mainly clean, but do contain some inclusions, principally graphite and insoluble silicides. Several of these silicides have a melting temperature below the melting point of silicon and can have a detrimental effect on bend strength at elevated temperatures. By comparison, the largely coherent epitaxial boundaries contain similar inclusions but do not seem to be weakened by them, suggesting that some other factor must also be important. Since most grain boundaries intersect regions of residual silicon, one possibility is a stress concentrating effect at the point where the SiC:SiC grain boundaries meet the silicon. This would be greatly enhanced by the presence there of low melting point silicides. For example, a flaw found at "A" in Fig. 9a will have a wedging effect on the adjacent grain boundary. The actual SiC:Si interfaces are also a source of weakness (in fact nucleation sites for cracks) but further study of their exact nature is required for this behaviour to be understood. They seem to act as nucleation sites for the solidifying silicon (with a definite orientation relationship), but the exact nature of this is not clear. There is some evidence for a thin amorphous film, but this also is not yet conclusive.

8.6. Texture

Although there is no direct crystallographic texture in the material, it is the crystallographic control of cleavage of the original SiC that produces the observed anisotropy in MOR data. The actual loss of strength comes from an effective increase in grain size (in a particular direction), and hence an increase in the weak SiC:Si interface length. However, the bulk strength can also be affected by various "macro-defects", such as nodules and silicon-filled cracks. If these are not eliminated (by careful processing), they totally dominate the mechanical properties.

9. Conclusions

Careful microstructural examination of fully reacted specimens, together with studies of a sequence of specimens from interrupted reaction-bonding experiments and other special samples, have allowed us to explain the microstructural evolution in reaction-bonded silicon carbides. Furthermore, a range of features of importance in the final microstructure have been fully characterized.

The highly localized nature of the C + Si reaction has been confirmed and the peak temperature at the reaction front has been shown to be high enough (~ 2000° C for ~ 4 min) to allow the $\beta \rightarrow \alpha$ transformation to go to virtual completion in the epitaxial overlayer. Although the C + Si reaction is rapid, the rate-controlling step is still uncertain, but it seems most likely to be carbon dissolution in the silicon.

The newly formed silicon carbide always grows as the β-polytype and nucleates either on the existing SiC grits or, less frequently, on the graphite or even homogeneously. The latter, finely dispersed SiC forms during the local cooling down of the liquid silicon immediately behind the reaction-front and thus never experiences sufficient thermal activation to transform to α-SiC.

The nucleation of new β-SiC on the existing grit particles has been demonstrated together with the progressive coalescence of these nuclei to form a single-crystal epitaxial deposit. This coalescence can lead to the deposit appearing "serrated" or "dendritic" and can produce faceted SiC:SiC grain boundaries when the epitaxial deposits from adjacent grains impinge. The growth morphology of the individual developing nuclei, together with the morphology of the epitaxial deposit as a whole, corresponds to the β (cubic) SiC polytype with preferred $\{1\,1\,1\}$, $\{1\,1\,0\}$ and $\{1\,0\,0\}$ growth planes. The mutual alignment of the nuclei on each grit particle is probably controlled by epitaxial nucleation on the $\{0\,0\,0\,1\}$ steps and ledges of each particle.

A remarkable feature of the reaction-bonding process is the ability of the silicon to carry impurities insoluble in SiC up the billet leaving some of them in the silicon extrusions finally left on the specimen surface. This, coupled with the removal of the silica layer on the original grits by reaction with the carbon, results in a general cleanliness of the vast majority of the grain boundaries and interfaces present. Thus, most SiC:SiC grain boundaries are strongly bonded by a thin (~ 1 nm) layer of amorphous silicon carbide. Occasionally, silicides and other impurities are trapped in grain boundaries and epitaxial interfaces and appear instrumental in controlling the high temperature strength of the compact. The SiC:Si interfaces, though apparently basically coherent, experimentally appear to be weak and need further investigation to allow fuller understanding of their role in mechanical property determination.

Soluble impurities – primarily aluminium and perhaps nitrogen – are incorporated into the newly formed silicon carbide and appear responsible for the secondary electron image contrast in the SEM. However, the explanation of the contrast is the opposite of the suggestion made by Sawyer and Page [7] in that it is the aluminium-rich material which images brightest. Any further role of nitrogen is as yet undetermined.

Shape anisotropy, principally governed by the $\{1\,1\,\bar{2}\,0\}$, $\{1\,0\,\bar{1}\,0\}$ and $\{0\,0\,0\,1\}$ cleavage morphology of the original SiC particles, has been shown to control the observed mechanical anisotropy of various types of reaction-bonded material depending upon the green compact forming route used. Not only does the resultant grain size vary in different directions but the alignment of the residual silicon regions controls the observed anisotropy in MOR.

Acknowledgements

The authors are grateful to Professor R. W. K. Honeycombe and subsquently Professor D. Hull, for provision of laboratory facilities. J. N. N. acknowledges the tenure of an SERC Case Studentship in collaboration with UKAEA Springfields, who supplied materials and controlled-preparation facilities. The authors would also like to thank Mr P. Kennedy and Mr J. O. Ware of UKAEA for their interest and assistance, and members of the Cambridge Tribology Group for helpful discussions. The following are also thanked: B. Riley (Auger Analysis, UKAEA), Dr K. Knowles (HREM), Mr J. Reich and Mr J. Davies (equipment maintenance), Miss A. Beckett (Quantimet), Mr M. Stocker and Mr S. Revell (SEM/TEM), and Mr A. Harris (LIMA).

References

1. P. KENNEDY and J. V. SHENNAN, "Silicon Carbide 1973", Proceedings of Conference, Miami Beach, September 1973, edited by R. C. Marshall, J. W. Faust, Jr and C. E. Ryan (University of South Carolina Press, Columbia, South Carolina, USA, 1974) p. 359.
2. M. G. S. NAYLOR, PhD thesis, University of Cambridge (1981).
3. P. POPPER, in "Special Ceramics" (Heywood, London, 1960) p. 209.
4. C. W. FORREST, P. KENNEDY and J. V. SHENNAN, in "Special ceramics 5" (British Ceramics Research Association, Stoke-on-Trent, 1972) p. 99.
5. L. S. RAMSDELL, *Amer. Mineral.* **32** (1947) 64.
6. H. SATO, S. SHINOZAKI, M. YESSIK and J. E. NOAKES, "Silicon Carbide 1973", Proceedings of Conference, Miami Beach, September 1973, edited by R. C. Marshall, J. W. Faust, Jr and C. E. Ryan (University of South Carolina Press, Columbia, South Carolina, USA, 1974) p. 222.
7. G. R. SAWYER and T. F. PAGE *J. Mater. Sci.* **13** (1978) 885.
8. A. H. HEUER, G. A. FRYBURG, L. U. OGBUJI and T. E. MITCHELL, *J. Amer. Ceram. Soc.* **61** (9/10) (1978) 406.
9. T. F. PAGE and G. R. SAWYER, *J. Mater. Sci.* **15** (1980) 1850.
10. L. U. OGBUJI, T. E. MITCHELL and A. H. HEUER, *J. Amer. Ceram. Soc.* **64**(2) (1980) 100.
11. J. N. NESS and T. F. PAGE, *Bull Mineral.* in press.
12. B. M. TUROVSKII and I. I. IVANOVA, *Inorg. Mater. (USA)* **10** (1974) 1809.
13. R. I. SCACE and G. A. SLACK, *J. Chem. Phys.* **30**(6) (1959) 1551.
14. R. C. ELLIS, in "SiC – A High Temperature Semiconductor" (Pergamon Press, Oxford, 1960) p. 124.
15. G. G. GNESIN and A. I. RAICHENKO, *Porosch. Met.* **13**(5) (1973) 35.
16. D. H. KIRKWOOD and J. CHIPMAN, *J. Phys. Chem.* **65** (1961) 1082.
17. N. W. JEPPS and T. F. PAGE, *J. Cryst. Growth* **7** (1983) 259.
18. D. E. NEWBURY, private communication (1984).
19. J. N. NESS, PhD thesis, University of Cambridge (1985).
20. P. KENNEDY, private communication (1982).
21. E. N. MOKHOV, B. S. MAKHMUDOV, M. N. USMANOVA and G. F. YULDASHEV, *Sov. Tech. Phys. Lett.* **8(3)** (1982) 163.
22. R. RUH and A. ZANGVIL, *J. Amer. Ceram. Soc.* **65** (1982) 260.
23. N. W. JEPPS, T. F. PAGE and W. M. STOBBS, in

"Grain Boundaries In Ceramics", Proceedings of Materials Research Societies, Vol. 5 (Elsevier, London, 1982) p. 45.

24. D. R. CLARKE, *Ultramicroscopy* **4** (1979) 33.
25. O. L. KRIVANEK, T. M. SHAW and G. THOMAS, *J. Appl. Phys.* **50**(6) (1979) 4223.
26. J. N. NESS, W. M. STOBBS and T. F. PAGE, in preparation.
27. T. F. PAGE, G. R. SAWYER, O. O. ADEWOYE and J. J. WERT, *Proc. Brit. Ceram. Soc.* **26** (1978) 193.
28. M. G. S. NAYLOR and T. F. PAGE, *J. Microsc.* **130** (1983) 345.
29. B. RALPH, P. R. HOWELL and T. F. PAGE, *Phys. Status Solidi* (*b*) **55** (1973) 641.
30. J. P. GOLIGHTLY, *Can. Mineral.* **10** (1969) 105.
31. A. J. DEKKER, in "Solid-State Physics" (Macmillan, London, 1958).
32. E. LIFSHIN and R. C. DEVRIES, Proceedings of the 7th Conference on Election Probe Analysis, San Francisco, 1972 (Microbeam Analysis Society, San Francisco, California, USA) p. 18a.

Received 20 June
and accepted 10 July 1985